Large-scale molecular dynamics simulations of dense plasmas: The Cimarron Project

Frank R. Graziani [a],*, Victor S. Batista [c], Lorin X. Benedict [a], John I. Castor [a], Hui Chen [a], Sophia N. Chen [a], Chris A. Fichtl [b], James N. Glosli [a], Paul E. Grabowski [b], Alexander T. Graf [a], Stefan P. Hau-Riege [a], Andrew U. Hazi [a], Saad A. Khairallah [a], Liam Krauss [a], A. Bruce Langdon [a], Richard A. London [a], Andreas Markmann [c], Michael S. Murillo [b], David F. Richards [a], Howard A. Scott [a], Ronnie Shepherd [a], Liam G. Stanton [a], Fred H. Streitz [a], Michael P. Surh [a], Jon C. Weisheit [d], Heather D. Whitley [a]

[a] Lawrence Livermore National Laboratory, Livermore, CA 94550, USA
[b] Computational Physics Group, Los Alamos National Laboratory, Los Alamos, NM 87545, USA
[c] Department of Chemistry, Yale University, New Haven, CT 06520-8107, USA
[d] Department of Physics and Astronomy, University of Pittsburgh, Pittsburgh, PA 15260-8709, USA

ARTICLE INFO

ABSTRACT

We describe the status of a new time-dependent simulation capability for dense plasmas. The backbone of this multi-institutional effort — the Cimarron Project — is the massively parallel molecular dynamics (MD) code "ddcMD," developed at Lawrence Livermore National Laboratory. The project's focus is material conditions such as exist in inertial confinement fusion experiments, and in many stellar interiors: high temperatures, high densities, significant electromagnetic fields, mixtures of high- and low-Z elements, and non-Maxwellian particle distributions. Of particular importance is our ability to incorporate into this classical MD code key atomic, radiative, and nuclear processes, so that their interacting effects under non-ideal plasma conditions can be investigated. This paper summarizes progress in computational methodology, discusses strengths and weaknesses of quantum statistical potentials as effective interactions for MD, explains the model used for quantum events possibly occurring in a collision, describes two new experimental efforts that play a central role in our validation work, highlights some significant results obtained to date, outlines concepts now being explored to deal more efficiently with the very disparate dynamical timescales that arise in fusion plasmas, and provides a careful comparison of quantum effects on electron trajectories predicted by more elaborate dynamical methods.

© 2011 Elsevier B.V. All rights reserved.

1. Introduction and overview

Hot dense radiative (HDR) plasmas common to inertial confinement fusion (ICF) and stellar interiors have high temperature (a few hundred eV to tens of keV), high density (a few to hundreds of g/cc) and high pressure (hundreds of megabars to thousands of gigabars). In addition to the extreme conditions defining HDR plasmas, the fact that they can be composed of low-Z (p, D, T, He^3, …) and high-Z ions (C, Kr, Xe, Au, …) means there is a complex interplay of atomic, radiative and thermonuclear processes that need to be accounted for. Some HDR regimes relevant to this work are located in the temperature–density plot, Fig. 1.

Information that elaborates various properties of and physical processes in high energy density matter can be found in recent proceedings of the conference series "Strongly Coupled Coulomb Systems" and "Radiative Properties of Hot, Dense Matter," as well as the monograph "The Physics of Inertial Fusion" [1].

To be more specific, developing an understanding of HDR plasmas means understanding the physics of high-Z ions in various states of ionization, with light ions undergoing thermonuclear reactions; electrons in various degrees of degeneracy; non-thermal charged particles depositing energy and momentum; and photons undergoing scattering, absorption and emission. This is the challenge confronting those who develop radiation–hydrodynamic codes for astrophysical and ICF applications, their goal being a robust and accurate tool that can be used to design experiments, analyze data and explain observations. Due to the complexity of HDR plasmas and the shortage of validating data in the regimes of

* Corresponding author.
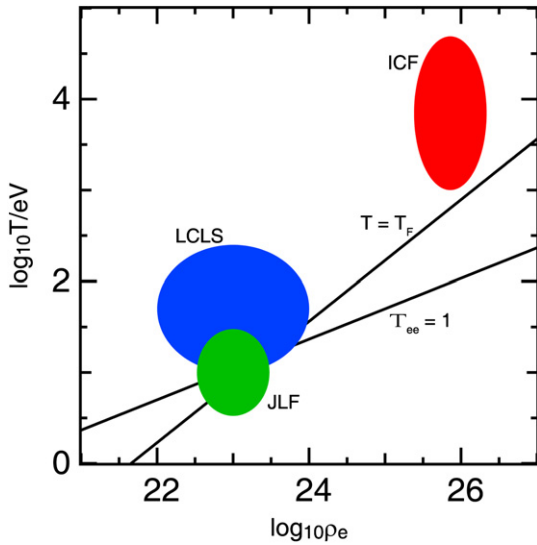E-mail address: graziani1@llnl.gov (F.R. Graziani).

Fig. 1. The various domains of non-degenerate vs. degenerate matter, and weak vs. strong plasma coupling in ρ_e, T space are compared with the prevalent conditions in ICF, LCLS and JLF plasmas. Abscissa: electron density ρ_e in electrons/cm^3; ordinate: temperature T in eV.

interest, computational physicists resort to the best available theoretical models based on kinetic theory of energy exchange, EOS, transport coefficients and stopping power. The theories often depend on ad-hoc cut-offs, ignore strong scattering or bound states, and are vague about treating multiple species. In particular, it is not obvious how to treat plasma mixtures where, for example, the low-Z component might be weakly coupled but the high-Z component, strongly coupled.

Recent advances in high performance computing have opened another avenue to a deeper understanding of HDR plasmas and at the same time provided insight into the accuracy of kinetic theory. Particle-In-Cell (PIC) [2,3] and Molecular Dynamics (MD) [3] methods have provided the capability of creating virtual non-equilibrium plasmas, whose properties can be investigated and diagnosed in ways analogous to those an experimentalist uses to study a plasma in a laboratory. The virtual plasma method also provides insight into the micro-physical foundations of widely accepted theories. And, since strong coupling is not an issue per se, it provides insight into plasma regimes where current kinetic theory is not valid.

This paper reviews the Cimarron project, which is using the massively-parallel MD code ddcMD to investigate numerous time-dependent phenomena in multi-species HDR plasmas. Why MD? The HDR plasmas of interest are highly collisional. While both PIC and MD can be used [4], MD includes Coulomb collisions naturally whereas PIC has to include some sort of collisional model to account for short-range collisions. Thus, MD provides greater accuracy and efficiency for strong collisions. Coulomb forces in ddcMD code are computed using the particle–particle–particle–mesh method (PPPM or P^{3}M) [3]. In this method long-range force terms are calculated with a particle-mesh (PM) technique (similar to PIC) while short-range force terms are calculated with explicit parti-cle–particle (PP) interactions. The strength of MD is also its biggest challenge: time scales are dominated by the short intervals between electron–electron collisions. (New hybrid approaches for tackling this problem will be discussed at the end of this paper.) MD is also limited by the number of particles in a computational box and hence for HDR plasmas it is restricted to rather small length scales. Limi-tations aside, given accurate pair potentials ddcMD provides an

accurate numerical solution to the many-body classical particle dynamics. Key computational features of this code are summarized in Section 2.

By far, most MD codes do not explicitly treat electrons and applying MD to a plasma requires much more thought than simply including the electrons as addtional classical particles in the simulation. Actual electron–electron and electron–proton colli-sions involve quantum interference and diffraction effects at small distances. At the same time, there is a large-distance collective effect which manifests itself as Debye screening. This dual-scale phenomenon is exhibited in the Coulomb logarithm [5] as the ratio of the Debye length to the thermal de Broglie wavelength. To characterize these effective interaction features, quantum statis-tical potentials (QSPs) [6] modify the Coulomb potential at short range with quantum effects while leaving the long-range behavior intact. Although QSPs have been used with great success, they are, by necessity, only approximations for the quantum dynamics of real electrons and it is not known quantitatively how well they repro-duce processes relying on aspects of quantum dynamics. QSPs are discussed in detail in Section 3.

The use of simulations to understand the micro-physics of HDR plasmas raises the question of how one validates and tests MD. Our strategy here is two-pronged: (1) make comparisons with other theoretical/computational results in regimes of moderate density and Coulomb coupling strength; (2) make comparisons with experiments that probe regimes where our code should be valid. Even though these comparisons are being made in regimes not necessarily of highest interest from an HDR plasma point of view, they provide confidence in our simulation capability when careful extrapolations to HDR plasma conditions are undertaken.

Now, in practice, the former kind of comparisons noted above tend to focus on fully ionized plasmas, and the latter, on partially ionized plasmas. Thus, in addition to fusion and free–free radiation events in burning plasmas, MD simulations of plasmas must also be able to include the atomic kinetics of ionization and recombination for ions of heated target materials. Section 4 describes the model we use to handle quantum processes in a (classical) MD simulation that incorporates QSPs. For certain test cases mentioned there, this approach is still problematic.

Section 5 presents a representative set of results for fully ionized plasmas. These illuminate important features of static (mean) and dynamic correlations, electron–ion energy exchange and stopping power under HDR conditions.

The two experimental efforts within the Cimarron project are described in Section 6, together with the current state of our related validation work. Briefly, (1) experiments have been performed at the Jupiter Laser Facility (JLF) of proton stopping in heated, well-characterized carbon targets. (2) Experiments are also being per-formed at the Linac Coherent Light Source (LCLS). The goal is to heat solid density matter volumetrically and isochorically using the ultra-short pulse 2 keV radiation beam. The LCLS pulse is also used to measure the plasma's dynamic structure factor $S(\mathbf{k}, \omega)$.

Given the significant capabilities of molecular dynamics for analyzing non-equilibrium behavior of HDR plasmas, improve-ments in our MD approach continue to be made. In Section 7, we look to the future and discuss other methodologies that can be melded with MD to augment its core capabilities. Under consider-ation are wave-packet MD, momentum-dependent QSPs, and kinetic-theory MD (wherein electrons are treated via a quantum kinetic equation while the ions are still treated by classical MD). And, we are exploring the use of density-functional theory for situations that do not require explicit treatment of electron dynamics.

In Section 8, we return to QSPs, and investigate stringent tests using exact solutions of the time dependent Schrodinger equation for electron–ion scattering. These studies reveal an important issue

with QSPs that has received little attention in the literature to date − we must be cautious in the manner in which we interpret what the potentials yield.

Finally, in Section 9 we discuss future developments underlying the physics capability of the MD code. One thrust is moving beyond QSPs and thereby improving the micro-physics of the electron−ion interaction. The other closely related thrust is enhancing the ability of the MD code to simulate numerous, tightly coupled physical processes, especially those in HDR plasmas undergoing thermo-nuclear burn.

2. Computational methods

2.1. Molecular dynamics methods

Molecular dynamics (MD) is a discrete particle simulation method developed in the 1950's by Alder and Wainwright [7]. Though the name suggests and it certainly has been used to study molecular systems the method has a much broader application: it has been used to study atomic systems, macro particles and even nuclear systems with explicit hadrons. The focus of this paper is how MD is used to simulate hot plasmas in which all the ions and electrons are treated as explicit particles.

The molecular dynamics method is simply the numerical integration of equations of motion of a set of particles that are interacting via some potential energy function V. Typically the equations of motion are the classical Newton's equation

$$\frac{d^2 r_i}{dt^2} = \frac{f_i}{m}, f_i = -\nabla_i V \tag{1}$$

and V is a function only of the particle positions. That is, $V = V(r_1,\ldots,r_N)$. However generalizations to both the equations of motion and potentials to include relativistic, quantum and momentum dependent effects can all be explored.

The strength of the MD method is that once the potential energy function V and the equations of motion have been chosen the evolution of the system is completely defined. This evolution can be tracked at the smallest relevant time and length scales and all particle correlations are measurable. One might say that a virtual laboratory has been created where all the finest time and length scales can be observed.

The errors associated with MD are three-fold: potential energy model, sampling and integration. The simplest of these errors to understand and control is the integration error. This error is associated with the numerical integration scheme and controlled by the size of the time step, h, used. For instance consider one of the most common numerical integration methods, the velocity−Verlet algorithm [8];

$$r_i(t+h) = r_i(t) + v_i(t)h + \frac{1}{2}\frac{f_i}{m_i}h^2 + O\left(h^3\right)$$
$$v_i(t+h) = v_i(t) + \frac{1}{2}\frac{f_i(r(t)) + f_i(r(t+h))}{m_i}h + O\left(h^3\right) \tag{2}$$

Though a relatively low order method ($O(h^3)$) velocity Verlet preserves (up to roundoff error) the symplectic [9] symmetry of Hamilton's equation (the equations of motions). One property of symplectic integrators, and the reason we chose to use velocity Verlet in this work, is that the long-time energy drift for a micro-canonical simulation is very small. Often, it is desirable to control other average quantities besides the total energy. For instance temperature or pressure [10]. There are many methods (Andersen [11], Berendsen [12], Nose-Hoover [13], Langevin [14]) to control temperature in an MD simulation. Temperature control is of particular importance for this work and we have chosen to use the Langevin method. The Langevin method is a stochastic method where the equation of motion for the velocity in Eq. (2) is modified by adding a small random (white) noise and a frictional force directly proportional to v_i:

$$m\frac{d^2 r_i}{dt^2} = f_i - \frac{mv_i}{\tau} + \sqrt{\frac{6mT}{\tau}}g(t) \tag{3}$$

where $g(t)$ is a three-vector of independent random variables of unit variances. This particular choice of noise and friction term ensure that the fluctuation−dissipation theorem is obeyed, thereby guaranteeing "NVT" statistics. The time constant τ is somewhat arbitrary, and is adjusted to provide a suitable rate of thermal equilibration in the simulation.

The sampling error is associated with the number of time steps that are completed and hence the total physical time simulated. Normally MD is used to explore typical properties of a system. The longer the simulation time the greater number of states explored and hence the better the sampling. Though in principle this error is controllable by increasing the simulation time, many systems can have very long time processes and it may be very computationally demanding to sample sufficiently.

Perhaps the greatest challenge for reliable MD simulations is to develop high quality potential energy models. The models may be simple pair potentials such as Lennard−Jones [15] and pure Coulomb or complex many body models such as MGPT [16] or bond-order [17−19]. Computational intensity may vary from thousands to millions of floating point operations per particle per time step. Unfortunately, even the most complex many body atomic model potentials sometimes fail to capture all the needed physics and quantum mechanical methods must be used to evaluate the potential energy.

2.2. Domain decomposition in ddcMD

In parallel MD codes it is necessary to divide the simulation volume into domains each of which is assigned to a computer core (i.e., an MPI task). Because particles near domain boundaries interact with particles in nearby domains, internode communication is required to exchange particle data between domains. The surface-to-volume ratio of the domains and the choice of potential set the balance of communication to computation.

The domain-decomposition strategy in ddcMD allows arbitrarily shaped domains that may even overlap spatially. Also, remote particle communication between nonadjacent domains is supported whenever the interaction length exceeds the domain size. A domain is defined only by the position of its center and the collection of particles that it "owns". Particles are initially assigned to the closest domain center, creating a set of domains that approximates a Voronoi tessellation. The choice of the domain centers controls the shape of this tessellation and hence the surface-to-volume ratio for each domain. The commonly used rectilinear domain decomposition employed by many parallel codes is not optimal from this perspective. A better surface-to-volume ratio in a homogeneous system is achieved if domain centers form a bcc, fcc, or hcp lattice, which are common high-density packing of atomic crystals.

In addition to setting the communication cost, the domain decomposition can also control load imbalance. Because the domain centers in ddcMD are not required to form a lattice, simulations with a non-uniform spatial distribution of particles such as occurs with high-Z impurities can be load balanced by an appropriate non-uniform arrangement of domain centers. The flexible domain strategy of ddcMD allows for the migration of the computational work between domains by shifting the domain

centers. As any change in domain center positions affects both load balance and the ratio of computation to communication, shifting domain centers is a convenient way to optimize the overall efficiency of the simulation. Given an appropriate metric (such as overall time spent in MPI barriers) the domains can be shifted on-the-fly in order to maximize efficiency.

2.3. Dealing with Coulomb interactions

When selecting the potential energy function to describe a plasma it is tempting to simply treat the electrons and ions as bare Coulomb particles; unfortunately, this is ill-advised on several grounds. From a practical point of view, one is faced with the "Coulomb Catastrophe Problem" in which electrons will eventually recombine into classical bound states that are infinitely deep. Not only does this provide an arbitrarily large amount of energy, the time step must be arbitrarily small to resolve the motion of an electron that is deep in the attractive Coulomb well. Other issues arise from a physics perspective. We know that density fluctuations are suppressed at wavelengths shorter than the thermal de Broglie wavelength, which depends upon $\hbar$. This affects the static and dynamic structure factors discussed in Sections 5.1 and 5.3. Also, for some applications of interest, such as warm dense matter (including fast ignition) experiments, the electrons can be partially degenerate. Finally, the electrons also display important diffractive effects, which modify the screening properties and, in the extreme, even the proper formation of bound states.

To account for all of these issues, the workhorse method has been the use of Quantum Statistical Potentials (QSPs). The use of QSPs was pioneered by Hansen and co-workers, who investigated a variety of equilibrium and non-equilibrium plasma properties [20–24]. Because the validity of QSPs impacts the believability of any MD simulation that incorporates them, the physics underlying QSPs is discussed in some detail in Section 3. Also discussed there is the important point that QSPs are rigorously derived only for equilibrium plasmas; hence, their applicability to non-equilibrium situations requires careful consideration.

Because QSPs modify the Coulomb potential only at short range (and only for the electrons) we are forced to confront the conditional convergence issues associated with a potential that behaves as $1/r$ at long range. Fortunately, a variety of well-known, accurate and efficient methods for calculating long-range electrostatic forces exists: Ewald summation, fast multipole methods [25], and real-space multigrid methods [26,27] to name a few. Here we limit the discussion to Ewald type methods, in particular the very efficient PPPM approach [3,28].

The idea behind an Ewald-type approach is to split the Coulomb interaction into a short-range term and a smooth long-range term. This can be accomplished by adding and subtracting to each charged particle a screening charge distribution centered at the particle location. For example if Gaussian screening charges are used

$$\rho_i(\mathbf{r}) \equiv q_i \left(\alpha^2/\pi\right)^{3/2} \exp\left(-\alpha^2(\mathbf{r}-\mathbf{r}_i)^2\right) \tag{4}$$

the Coulomb potential energy can be written as

$$V = \frac{1}{2}\sum_{i=1}^{N}\sum_{j\neq i}^{N}\left\{\frac{q_i q_j \text{erfc}\left(\alpha r_{ij}/\sqrt{2}\right)}{r_{ij}} + \int\int\frac{\rho_i(\mathbf{r})\rho_j(\mathbf{r}')}{|\mathbf{r}-\mathbf{r}'|}d\mathbf{r}d\mathbf{r}'\right\} \\ -\frac{\alpha}{\sqrt{2\pi}}\sum_{i=1}^{N}q_i^2. \tag{5}$$

The first term in this expression is short-ranged so it can be cut off at finite r and calculated in $O(N)$ time using standard MD techniques for short-ranged potentials such as neighbor lists or link cells. The QSP corrections can be easily incorporated into this term. The second term contains the long-range character of the interaction and gives rise to a smooth charge distribution $\rho(\mathbf{r})$ that can be solved efficiently in Fourier space. To enable the use of fast Fourier transforms (FFTs) we assign the charge density onto an appropriate mesh, with the mesh spacing δ. The third term is usually referred to as the self energy. Boundary conditions at infinity can lead to additional terms which vanish in our application. With appropriate choices made for the short range radial cut-off ($r_c \propto \alpha^{-1}$) and the resolution of the mesh used to solve the long range part, the PPPM method successfully reduces the overall scaling of the algorithm from $O(N^2)$ to $O(N\log N)$.

2.4. Scaling PPPM to large N systems

When applied to systems with a large number of particles on massively parallel computers, the respective scalability of the short- and long-range force terms is very different. For the long-range terms the global communication typically needed to compute three-dimensional FFTs poses a significant scaling challenge. To overcome this problem we have developed a heterogeneous decomposition strategy in which the available processes are divided into two subsets. One subset computes the short-range explicit pair forces, the other handles the terms involving FFTs. A detailed description of this method is available in Ref. [29]. These two subsets do not need to contain the same number of processors. In particular, the size of the FFT subset can be chosen to be a small fraction (typically 5–10%) of the available cores. This greatly reduces scalability demands placed upon the FFTs. In practice the relative sizes of the subsets is a run-time parameter that can be used to optimize the time-to-solution for a given problem.

To investigate weak scaling behavior we performed a series of runs using 232 to 278,528 tasks and approximately 9400 particles per task. In each run we set the number of mesh tasks to approximately 6% of the total number of tasks. We found that the value of α that minimized run time (for constant $\alpha\delta$) is a function of the number of tasks. For 232 tasks a minimum was found at $\alpha = 2.4$ and for 278,528, $\alpha = 2.063$. We have not optimized run time for each point in the weak scaling study, but rather have interpolated α from the smallest to the largest simulation.

Efficiency at full scale has fallen off by roughly 15% compared to perfect scaling. This is a considerable accomplishment considering that the number of tasks is nearly 300,000 while other PPPM implementations typically experience 30% fall off at task counts of 10,000–30,000 [30]. Hence, our heterogeneous decomposition strategy has extended the weak scaling range by a factor of nearly 10.

3. Quantum statistical potentials

3.1. Basic concepts

Statistical potentials have been used in studies of plasmas for many years, and details of their derivation can be found in Jones and Murillo [6] as well as references cited therein. Here, we review their derivation starting from the quantum partition function at finite temperature, $T = 1/\beta$ in energy units. In this case, a quantum system is described by the finite-temperature density matrix [31]. In the basis of the particle positions, $\{\mathbf{R}\}$, the density matrix can be written as

$$\rho(\mathbf{R}, \mathbf{R}'; \beta) = \sum_s \Psi_s(\mathbf{R}) e^{-\beta E_s} \Psi_s^*(\mathbf{R}'), \tag{6}$$

where Ψ_s and E_s are the eigenfunctions and eigenvalues of the full system Hamiltonian. The partition function of the quantum system is the trace of the density matrix:

$$Q \equiv Tr\left(e^{-\beta \hat{H}}\right) = \int d\mathbf{R} \rho(\mathbf{R},\mathbf{R};\beta). \tag{7}$$

A semiclassical equation for the N-body system is obtained by multiplying the partition function by a particular form of unity [6],

$$\begin{aligned}
Q &= \frac{C}{C} \int d\mathbf{R} \rho(\mathbf{R},\mathbf{R};\beta) \\
&= \int \frac{d^{3N}p}{(2\pi\hbar)^{3N}N!} e^{\sum_i -\beta p_i^2/2m} \int d\mathbf{R} \frac{\rho(\mathbf{R},\mathbf{R};\beta)}{C}.
\end{aligned} \tag{8}$$

This expression shows that if an appropriate form of the second factor of Eq. (8) can be defined, the *quantum* partition function of Eq. (7) can be sampled through *classical* MD. The term $\rho(\mathbf{R},\mathbf{R};\beta)/C$ is analogous to the interaction term in classical MD. At the temperatures of interest in this study, determination of an accurate form of this second term is straightforward.

In general, we cannot solve Eq. (6) exactly for an N-body system. An approximation that is commonly used in path integral Monte Carlo is to factorize the Hamiltonian to obtain a product of terms that can be calculated exactly [32]. At very high temperature, this type of factorization of the density matrix becomes very accurate. As $T \to \infty$, $\beta \to 0$, hence the partition function can be written as a product of the kinetic and potential terms [33],

$$e^{-\beta\hat{H}} \approx e^{-\beta\hat{K}}e^{-\beta\hat{V}}, \tag{9}$$

where the kinetic term contains contributions from all particles in the N-body system,

$$\hat{K} = -\sum_{i=1}^{N} \frac{\hbar^2}{2m_i}\nabla_i^2, \tag{10}$$

and $\hat{V}$ is the total interaction. The kinetic term can thus be written as a product of N free-particle kinetic terms, the form of which is exactly known [32]. Since the interaction potentials relevant to the systems we study here are written in terms of sums over pair interactions, an accurate form of the interaction potential term in the density matrix is obtained by writing the potential term as a product of the pair density matrices for each pair of particles. The density matrix thus takes the form

$$\rho(\mathbf{R},\mathbf{R}';\beta) \approx \left[\prod_{i=1}^{N} \rho_F(\mathbf{r}_i,\mathbf{r}_i';\beta)\right]\left[\prod_{i<j} \frac{\rho_2(\mathbf{r}_{ij},\mathbf{r}_{ij}';\beta)}{\rho_F(\mathbf{r}_{ij},\mathbf{r}_{ij}';\beta)}\right], \tag{11}$$

where

$$\rho_F(\mathbf{r}_i,\mathbf{r}_i';\beta) = \left(\frac{2\pi\beta\hbar^2}{m_i}\right)^{-3/2}\exp\left[-\frac{m_i|\mathbf{r}_i-\mathbf{r}_i'|^2}{2\hbar^2\beta}\right] \tag{12}$$

is the free particle density matrix and $\rho_2(\mathbf{r}_{ij},\mathbf{r}_{ij}';\beta)/\rho_F(\mathbf{r}_{ij},\mathbf{r}_{ij}';\beta)$ is the non-ideal part of the pair density matrix for each pair of particles ij; this, we discuss below. This approximation results in errors of order β^3, which is quite small at the temperatures in this study [32].

Returning to Eq. (8) and having obtained an accurate expression for $\rho(\mathbf{R},\mathbf{R}';\beta)$, an appropriate expression for C must be defined. At very high temperatures, the quantum and classical momenta are equal, hence we define $C = \prod_i \rho_F(\mathbf{r}_i,\mathbf{r}_i';\beta)$. Then the final expression for the partition function becomes

$$Q = \int \frac{d^{3N}p}{(2\pi\hbar)^{3N}N!} e^{\sum_i -\beta p_i^2/2m} \int d\mathbf{R} \prod_{i<j} \frac{\rho_2(\mathbf{r}_{ij},\mathbf{r}_{ij};\beta)}{\rho_F(\mathbf{r}_{ij},\mathbf{r}_{ij};\beta)}. \tag{13}$$

It follows that we can define the effective, temperature dependent statistical Coulomb potential for a pair of particles, $U^C(r_{ij},\beta)$, from the second factor in Eq. (13),

$$U^C(r_{ij},\beta) = -\frac{1}{\beta}\log\left[\frac{\rho_2(\mathbf{r}_{ij},\mathbf{r}_{ij};\beta)}{\rho_F(\mathbf{r}_{ij},\mathbf{r}_{ij};\beta)}\right]. \tag{14}$$

In order to calculate this quantity, one must calculate the diagonal elements of the pair density matrix. The diagonal part of $\rho_F(\mathbf{r}_{ij},\mathbf{r}_{ij};\beta)$ is a constant, $(2\pi\beta\hbar^2/\mu_{ij})^{-3/2}$, where μ_{ij} is the reduced mass for the pair of particles. For a two-body (pair) problem, such as electron–electron, nucleus–electron, or nucleus–nucleus scattering, the Schrödinger equation can be solved exactly so that all $\{\Psi_s\}$ and $\{E_s\}$ are known, and $\rho_2(\mathbf{r}_{ij},\mathbf{r}_{ij}';\beta)$ can be computed exactly from Eq. (6). The only numerical difficulty comes from the fact that at very high temperatures the number of states that must be included in the sum becomes prohibitively large. For Coulomb systems, an efficient method for calculating the pair density matrix was developed by Pollock [34]. We use both the Pollock method and the matrix squaring method [32,35,36] to compute the exact pair densities used in this study.

In order to make the derived statistical potentials amenable to use in our classical MD code, we then fit the potentials to an analytical form previously derived by Kelbg [37] and improved by Filinov et al. [38],

$$U(r_{ij},\beta) = \frac{q_iq_j}{r_{ij}}\left[1-e^{-\left(\frac{r_{ij}}{\lambda_{ij}}\right)^2}+\sqrt{\pi}\frac{r_{ij}}{\lambda_{ij}\gamma_{ij}}\left(1-\mathrm{erf}\left[\gamma_{ij}\frac{r_{ij}}{\lambda_{ij}}\right]\right)\right]. \tag{15}$$

Here λ_{ij} and γ_{ij} are treated as temperature dependent fitting parameters. For the high temperature hydrogen studies presented here, $\gamma_{ij} = 1$ and λ_{ij} is the thermal de Broglie wavelength, $\lambda_{ij}^2 = \frac{\hbar^2\beta}{2\mu_{ij}}$. A comparison of the computed statistical potentials and their fits for an electron–proton pair is shown in Fig. 2.

3.2. Pauli potential

Next, we consider various formulations of the Pauli potential. The Pauli potential was, in fact, the first QSP to be developed. Shortly after the development of quantum mechanics, Uhlenbeck and Gropper [39] sought a method by which one could use the equation of state to distinguish Bose and Fermi gases. In doing so, they noted that the usual classical potential used in the partition function should be replaced by

$$\begin{aligned}
U_{ee}(r) &= U_{ee}^C(r) - \beta^{-1}\ln(1 \pm \exp(-r^2/\Lambda_{UG}^2)) \\
&\equiv U_{ee}^C(r) + U_{UG}(r),
\end{aligned} \tag{16}$$

where the upper/lower sign is for bosons/fermions and $\Lambda_{UG} = \hbar/\sqrt{m_e\overline{T}}$. In what follows, we will only consider fermions. This result can be readily obtained exactly from the pair density matrix for two non-interacting plane waves with the appropriate symmetrization of the two-particle wavefunction. Because this result is obtained for two particles, it represents a low density approximation [6]; note that Eq. (16) does not have an explicit density dependence. Lado showed how to extend this result to the spin averaged case [40], which, for the electronic (spin-1/2 fermions) case, has the form
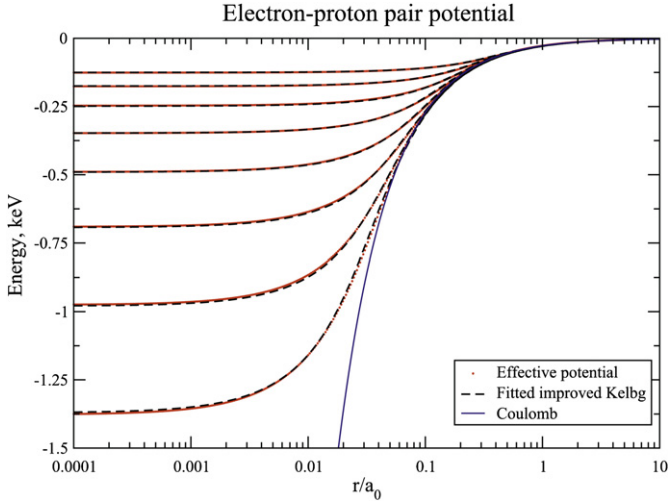
Fig. 2. Comparison of effective potentials for an electron-proton pair calculated from Eq. (14) (red) using the matrix squaring method. The fitted potential from Eq. (15) is shown as black dashed lines. The dashed blue curve is the Coulomb potential. The effective potential is shown for eight different temperatures (from top to bottom: T = 86 eV, 172 eV, 345 eV, 689 eV, 1.4 keV, 2.8 keV, 5.5 keV, 11 keV). (For interpretation of the references to colour in this figure legend, the reader is referred to the web version of this article.)

$$u_L^P(r) = -\beta^{-1}\ln\left(1 - \frac{1}{2}\exp\left(-r^2/\Lambda_H^2\right)\right), \tag{17}$$

where $\Lambda_H = \hbar/\sqrt{\pi m_e T} = \Lambda_{UG}/\sqrt{\pi}$.

Historically, the forms Eqs. (16) and (17) are not the most common in use. For example, Hansen and co-workers [20] used the form

$$u_H^P(r) = \beta^{-1}\ln(2)\exp\left(-[\pi\ln(2)]^{-1}r^2/\Lambda_H^2\right) \tag{18}$$

originally suggested by Deutsch, Minoo and Gombert [41,42].

Note that this result differs from Eq. (16); however, we see that Eq. (18) has been adjusted such that $u_H^P(0) = u_L^P(0)$ and $\lim_{r\to 0} r^{-1}du_H^P(r)/dr = \lim_{r\to 0} r^{-1}du_L^P(r)/dr$, while retaining a form with an analytic Fourier transform, which is useful in integral equations. Hansen and co-workers also use a diffraction potential quoted by Deutsch et al., originally suggested by Dunn and Broyles [43],

$$U_{ab}^C(r) = \frac{q_a q_b}{r}[1 - \exp(-r/\Lambda_D)]. \tag{19}$$

Different authors have used different definitions of Λ_H and Λ_D; our calculations with "Dunn-Broyles" potentials actually use Eqs. (18) and (19) with numerical coefficients taken to agree with Hansen [20].

Lado has further extended these forms to dense systems [40]. In this formulation, an integral equation must be solved numerically; this has been done, and a fit has been given [6] for ease of use. However, we must be cautious in extending the diffractive and Pauli potentials to higher order when they are treated separately. In the true electronic structure problem, these two aspects of quantum mechanics cannot be treated separately. Recently, an approach has been developed [44] that largely overcomes this shortcoming.

3.3. Limitations of quantum statistical potentials

Despite the fact that the QSPs appear as corrections to the real, physical potential, as in Eq. (16), their use in dynamical applications is questionable. It has been generally argued that one should not refer to these additional terms as potentials (or forces) [45], a point that has been emphasized in the context of dense plasma physics [6]. We find three important weaknesses with the QSP approach: (1) particle interactions are treated on average, not distinguishing slow from fast particles; (2) the quantum modifications do not account for changes in the shape of the wavefunction during a collision; and (3) Pauli blocking does not involve momentum eigenstates; rather, it appears as a separation in coordinate space. For these reasons, we have explored several alternatives to the QSPs that are closer to the true dynamical solution that we seek. These methods, which include momentum-dependent potentials, wave packet molecular dynamics, and kinetic-theory molecular dynamics, are described in Section 7; some informative electron trajectory comparisons are presented in Section 8 to quantify the first two weaknesses noted above.

4. Small ball description of atomic and nuclear physics

Classical molecular dynamics faces difficulty when it is necessary to consider quantum processes such as emission/absorption of X-ray photons, thermonuclear fusion or atomic ionization/recombination. At least when expressed in classical language, such quantum events are governed by probabilities and are not described by deterministic (classical) equations. At present our best method to deal with these situations is a hybrid Monte Carlo (MC)/ Molecular Dynamics (MD) scheme, dubbed "Small Ball" (SB).

Quantum or semiclassical cross-sections σ_x may be used to describe the various processes "x" that are considered to occur during a close collision. When the classical MD brings an electron-ion pair to within a specified, small distance R_B, control is passed to a subroutine that forms conditional probabilities $P\{x\}$, given by the expression

$$P\{x\} = \frac{\sigma_x}{\pi R_B^2}. \tag{20}$$

It is easy to enforce detailed balance on the process rates described by this algorithm. Moreover, this algorithm gives a prediction independent of the choice of the small-ball radius R_B, at least over a restricted range of radii: Insofar as the arriving particle flux is simply multiplied by the projected area of the small sphere, the radius R_B cancels out of the event rate. But, if too large a radius R_B is chosen, the sphere will frequently contain more than one target, making it necessary to devise some scheme to handle multi-center collision events. On the other hand, if too small a radius is chosen, the enhancement of flux at the sphere's surface, as represented by the pair distribution $g_{ei}(R_B) > 1$, will be incorrect. (Pair distributions are defined and discussed in Section 5.1.) This is because the QSPs and, hence, the pair distributions arising in the MD simulation have no knowledge of extended charge distributions about nuclei that are produced by their bound electron(s). Given these constraints, we believe that the inequalities

$$0.5a_i < R_B < 0.8a_i, \tag{21}$$

where $a_i = (3/4\pi\rho_i)^{1/3}$ is the Wigner–Seitz (ion-sphere) radius, bracket reliable choices of the SB radius for atomic processes.

The Small Ball method was first employed to calculate radiation generation in hot dense plasmas [46–48]. Here, Kramers' semi-classical cross-section σ_K is used to calculate radiation emission and absorption processes. MC tests decide the photon energy $\hbar\omega$ and decide between absorption and emission, guided by conditional probabilities obtained from the cross-section. The MD code predicts a radiation spectrum that relaxes to the expected black-body distribution. Work in progress resolves bremsstrahlung emission (absorption) into individual angular momentum contributions.

In order to provide a consistent treatment of all the various processes that can occur in a given electron-ion collision, the SB algorithm is being used for non-radiative scattering events, too. Present efforts are focused on the issue of charge-state distributions in dense, partially ionized matter produced by intense X-ray or proton beams (see discussion of experiments and relevant simulations in Section 6). To model plasma ionization with minimal atomic kinetics, we have adapted the bottleneck approximation [49], which requires one to keep track only of ionization and recombination events to/from a few low-lying states; bound–bound transitions (radiative or collisional) among these states are ignored, as are all transitions involving bound states above the bottleneck. The bottleneck itself is identified as the lowest state for which the radiative lifetime exceeds the (inelastic) collisional lifetime, and in a hydrogenic approximation this state has principal quantum number

$$n^* = \left[\frac{2.6 \times 10^{18} \text{cm}^{-3} Z^6}{\rho_e} \left(\frac{T}{13.6 eV} \right)^{1/2} \right]^{1/9}. \tag{22}$$

Atomic processes included, to date, are (1) electron impact ionization and its inverse, three-body recombination; (2) X-ray ionization and subsequent Auger transitions; (3) radiative recombination. We use a scaled Mott cross section for collisional ionization events [50]; it is reasonably accurate and, importantly, it is an expression differential in the energy of the ejected electron (information needed subsequently by the MD routines). This same energy information is also required for the calculation of three-body recombination probabilities. X-ray ionization is based on atomic subshell photoionization cross sections [51]. Auger events are determined by an MC step from the Auger lifetimes [52]. And, for radiative recombination, we use the Milne relation (detailed balance) to obtain ground state cross sections from accurate photoionization formulae. Cross sections for recombination to excited states (below the bottleneck) use hydrogenic formulae.

The bottleneck approximation works particularly well for these dense systems. Fig. 3 demonstrates the efficacy of this concept using Xe at an electron density of $\rho_e = 10^{26}$ cm^{-3}, conditions appropriate to ICF. The Xe was initialized with 10 bound electrons at $t = 0$. The evolution of the ionization state at a fixed temperature of 10 keV was calculated with the atomic kinetics code Cretin [53], using atomic models incorporating bound states up to a maximum principal quantum number n_{max}. Varying n_{max} from 2 to 10 produced only two discrete evolution tracks − for $n_{max} = 2$ (solid line) and for $n_{max} \geq 3$ (dashed line), in agreement with the estimate from Eq. (19) of $n^* = 2.5$. The concordance with the bottleneck approximation is partially due to continuum lowering, as only a few bound states exist for any giving ionization stage under these conditions. However, omitting continuum lowering from the series of calculations produces results which also strongly support the bottleneck approximation. For comparison purposes, the dotted curve in Fig. 3 shows the evolution for $n_{max} = 5$ in the absence of continuum lowering. The overall evolution remains similar to that for $n_{max} \geq 3$ with continuum lowering, but with differences that could impact spectroscopic predictions of some plasma simulations.

Test comparisons with Cretin show that the SB algorithm together with the bottleneck approximation yield credible results for solid-density plasmas. Fig. 4 shows the evolution of a carbon plasma with a density of 2.2 g/cm^3, held at a temperature of $T_e = 50$ eV, both with the atomic kinetics and the MC/MD code. These conditions are relevant to LCLS and JLF plasmas described in Section 6. The results in the lower part of Fig. 4 are for an initially singly-ionized plasma which collisionally ionizes. The dash–dotted
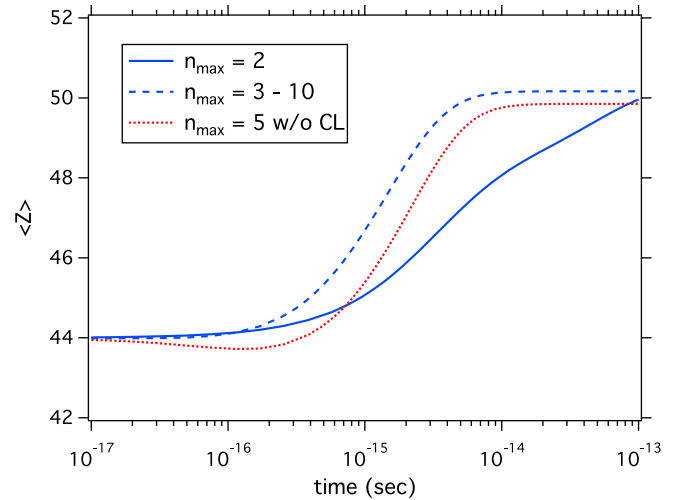

Fig. 3. Evolution in time of the mean charge state Z in a xenon plasma as computed with Cretin using different maximum principal quantum numbers, as described in the text.

curve shows the results from the MC/MD code, while the solid curve show atomics kinetics results which include both continuum lowering and excited states. The dashed curve shows results from the atomic kinetics code without continuum lowering. This more closely matches the physics currently incorporated in the MC/MD code. The agreement supports the concept of the SB algorithm, while emphasizing the importance of incorporating continuum lowering into SB. This task is in progress.

The upper portion of Fig. 4 is for a carbon plasma under the same conditions, which is initially completely stripped and proceeds to
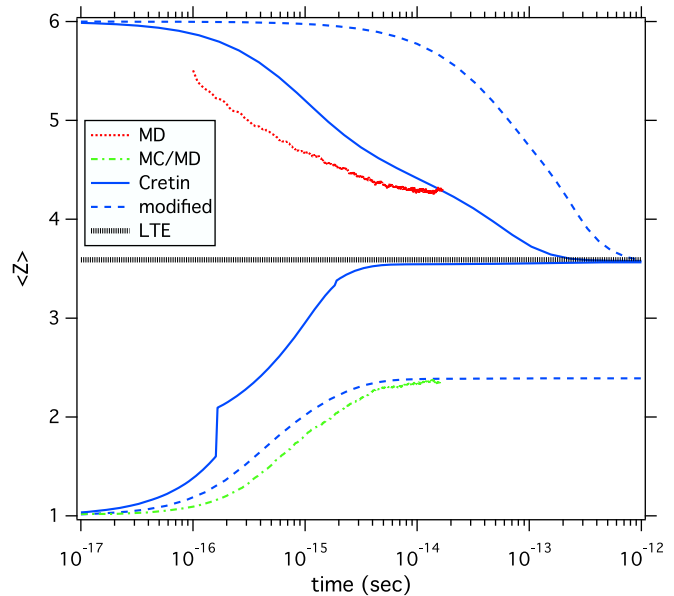

Fig. 4. Evolution in time of the mean charge state Z in a carbon plasma as computed with Cretin and with ddcMD. The lower part of the figure is for an ionizing plasma, demonstrating reasonable agreement between Cretin w/o continuum lowering (dashed curve) and ddcMD with the SB algorithm (dotted curve). The solid curve gives Cretin results including the effect of continuum lowering. The upper part of the figure is for a recombining plasma. Here, ddcMD is not using SB and the recombination proceeds classically, occurring much faster than the atomic kinetics results obtained by omitting any excited states (dashed curve). The solid curve shows Cretin results obtained including the effects of excited states.

recombine. The solid curve shows atomic kinetics results including excited states, while the dashed curve omits excited states. The omission of excited states is to more closely match the physics of the MD code, which here does not use the SB algorithm but evolves classically, with recombination measured by looking at the residence time of an electron around the nearest ion. The atomic kinetics results do include continuum lowering, which in this case affects the final charge state but not the recombination time scale. The comparison highlights a known, important issue — namely, the tendency of the classical charged system to exhibit prompt many-body relaxation whereby some electrons obtain energies well below that of the actual electron-ion ground state (this happens in spite of the use of "regularized" QSPs). Because this relaxation occurs on a timescale shorter than that characteristic of actual quantum recombinations, work is underway to develop a prescription that precludes the counting of spurious "classical recombinations".

The Small Ball algorithm also is being used to calculate thermonuclear reaction rates for DT plasmas. The constraints on the small ball radius, comparable with Eq. (20), are different in the nuclear case. The radius R_N should be chosen so that R_N is large compared with the (ion) de Broglie wavelength and the classical distance of closest approach of a DT pair in a head-on collision, and small compared with the ion sphere and Debye radii. This ensures that classical physics may safely be used for $r > R_N$, and that multiparticle effects may be neglected for $r < R_N$. By virtue of the latter, the correlations $g_{ii'}(r)$ have converged to a constant multiple of $\exp[-\beta U_{ii'}(r)]$. (The difference between the total correlation function h and the direct correlation function c has attained its $r \to 0$ limiting value.) Within this range of radii the calculated event rate discussed below is independent of the radius. Practical values of R_N are around 10^{-11} cm $\approx 10^{-2}a_i$, much smaller than for atomic processes. In a plasma with a sufficiently small Γ, the quantity $h_{ii'}(r) - c_{ii'}(r)$ is negligible everywhere, and the upper limit on R_N becomes moot.

A large-scale ddcMD run was made for a hydrogen plasma, and the events in which a proton pair approached within a distance R_N of each other were simply counted. Five million particles were included, and for this simulation we used $R_N = 0.01$ Å. The gas temperature was hot for a fusion plasma before ignition, 5 keV, but the density was a realistic 10^{25} cm^{-3}. The proton mass was scaled down by a factor 100 to increase the event rate. The simulation ran for 0.166 fs. The number of events counted was 77,115, which agrees within statistical error with the expected number based on the HNC pair correlation at $r = R_N$. This event rate could be turned into a fusion rate by applying the conditional probability $P\{x\}$, in which σ_x is taken to be the nuclear reaction cross section. Additional corrections are needed in the center-of-mass energy of the pair, and in the relation between impact parameter and angular momentum, owing to the potential energy of repulsion at $r = R_N$, before the SB algorithm can be applied. The conditional probability is found to be of order 10^{-6}, owing to the nuclear radius being much smaller than R_N. This emphasizes the fact that it is very challenging to obtain any fusion events unless MD simulations are performed for much longer times than those typically required for dense plasma studies.

5. A sampling of simulation results

5.1. Pair distribution functions and static equilibrium properties

Molecular dynamics simulations are widely used to compute macroscopic properties from microscopic models. Linear response theory and the fluctuation dissipation theorem can identify the relevant correlation functions for the desired property [54]. MD simulations for these microscopic quantities then include higher-order terms in the interaction potential, and so go beyond analytic perturbation theory. However, they are subject to statistical errors, which must be managed in practice by increasing the system size and computational effort. On the other hand, analytic methods are free of this complication and also provide insight and independent assessment of the numerical results.

For example, the thermodynamic potential for a system of N particles at temperature T,

$$\Phi = \langle \hat{\Phi} \rangle = \frac{3}{2}NT + \left\langle V - T\frac{\partial V}{\partial T} \right\rangle, \tag{23}$$

is calculated in terms of (canonical time- or ensemble-averaged) expectations of potential energies, $V_{\alpha\beta}$, summed over pairs of particles i and j of species α and β, respectively,

$$V = \sum_{i\alpha j\beta} V_{\alpha\beta}\left(r_{i\alpha j\beta}\right). \tag{24}$$

(Note that there is a correction to the internal energy for a temperature-dependent potential, $dV/dT \neq 0$, which comes from the derivative of the partition function, $Q = \int e^{-\beta H}$. For simplicity, this term is not evaluated here.)

In some cases, sampling errors can be mitigated by substituting different statistical mechanical identities for the same quantities. A direct approach to equation of state parameters like pressure, compressibility, and heat capacity would be to take numerical derivatives of $\Phi(T,V)$, but finite differencing compounds the variance from individual simulations. More sophisticated approaches relate thermodynamic parameters to the expectation of microscopic correlation functions. Pressure is obtained from the virial [3]:

$$P = T\frac{N}{\Omega} - \frac{1}{6\Omega}\left\langle \sum_{i\alpha j\beta}{}' \mathbf{F}_{i\alpha j\beta} \cdot \mathbf{r}_{i\alpha j\beta} \right\rangle \tag{25}$$

where Ω is the volume, and the $\mathbf{F}_{i\alpha j\beta} = -\boldsymbol{\nabla}V_{\alpha\beta}(\mathbf{r}_{i\alpha j\beta})$ are interparticle forces. Heat capacity is derived from fluctuations in internal energy:

$$C_V = \frac{\langle \hat{\Phi}^2 \rangle - \langle \hat{\Phi} \rangle^2}{T^2} - T\left\langle \frac{\partial^2 V}{\partial T^2} \right\rangle. \tag{26}$$

Note that evaluating $\partial\Phi/\partial T$ from Eq. (23) yields an additional correction from the T-dependence of V. Isothermal compressibility χ_T for the binary ionic fluid is obtained from the $k \to 0$ limit of density fluctuations ([21], Section 10.2, [55], Eq. 2.3.13):

$$\rho T\chi_T = \frac{-q_\alpha q_\beta}{x_\beta x_\beta \left(q_\alpha - q_\beta\right)^2} \lim_{k\to 0} S_{NN}(k); \tag{27}$$

this expression involves concentrations $x_\alpha = N_\alpha/N$, charges q_α, particle number density $\rho_N(k) = \sum_\alpha \rho_\alpha(k)$ and charge density $\rho_Z(k) = \sum_\alpha q_\alpha \rho_\alpha(k)$, plus the total number static structure factor $S_{NN}(k)$. For different combinations of number and charge,

$$S_{AB}(k) = \Omega \int d\mathbf{r}\, e^{-i\mathbf{r}\cdot\mathbf{k}} \langle \delta\rho_A(\mathbf{r})\delta\rho_B(0) \rangle, \tag{28}$$

in which A and B may be N or Z. Eq. (27) is obtained from a more complicated expression involving S_{NN}, S_{NZ} and S_{ZZ} and reduces to this form owing to charge neutrality [21, Chapt. 10].

The equilibrium properties described below are obtained from ensemble averages of instantaneous correlation functions. Consequently, thermostatted and mass-scaled simulations are possible,

wherein temperature is maintained by an external bath and the proton mass is reduced from the physical value. Classical coordinate distributions are independent of both modifications. Mass-scaling is advantageous because the time required to sample diverse phase space configurations is set by the slowest particles, while the simulation time step is limited by the fastest particles. Therefore, the dynamics are evaluated here with the proton mass reduced to $m_p/1000$ while the quantum statistical potentials for protons and electrons, V_{pp} and V_{ep}, are calculated using the physical mass, m_p.

Alternatively, the internal energy can be computed from the pair distribution functions and the potentials [54, Section 13-3], [20]:

$$\Phi = \frac{3}{2}NT + \sum_{\alpha\beta}\frac{\Omega\rho_\alpha\rho_\beta}{2}\int d\mathbf{r}g_{\alpha\beta}(r)\left[V_{\alpha\beta}(r) - T\frac{\partial V_{\alpha\beta}(r)}{\partial T}\right]. \quad (29)$$

Now,

$$g_{\alpha\beta}(r) = \frac{1}{\rho_\alpha\rho_\beta}\left\langle\sum_{i\alpha j\beta}'\delta(r - R_{i\alpha}(t_0))\delta\left(r - R_{j\beta}(t_0)\right)\right\rangle \quad (30)$$

involves an average over the simulation time, t_0. In this case the static structure factor is ([55], Eq. 2.3.6):

$$S_{\alpha\beta}(k) = \delta_{\alpha\beta} + \sqrt{\rho_\alpha\rho_\beta}\int d\mathbf{r}e^{i\mathbf{k}\cdot\mathbf{r}}\left(g_{\alpha\beta}(\mathbf{r}) - 1\right). \quad (31)$$

Such expressions are useful for analytic methods that obtain an approximate pair distribution function from the pair-potentials, like the hypernetted-chain (HNC) method [54]. Other expectation values can also be replaced by an integral over g(r), e.g.:

$$P = \frac{N}{\Omega}T - \frac{1}{6}\sum_{\alpha\beta}'\rho_\alpha\rho_\beta\int d\mathbf{r}r\frac{\partial V_{\alpha\beta}}{\partial r}g_{\alpha\beta}(r). \quad (32)$$

In the case of pressure, there is no T-dependent correction. There would be a density-derivative term if the QSPs were ρ-dependent, but the forms considered here are not.

Table 1 shows the internal energy, compressibility, and heat capacity for hydrogen plasmas in four different states. For comparison purposes, all of the calculations that are reported here exclude the corrections for the T-dependent potentials. Data are obtained by MD and HNC methods, using the Dunn–Broyles statistical potential for quantum diffraction and the Deutsch term for Pauli exclusion among electrons [20]. Only the excess values or corrections from ideal gas results are shown, otherwise these weak-coupling systems are dominated by the ideal gas behavior. The agreement is good for the weak coupling cases. Fig. 5 shows the pair distribution functions for one pressure/density case. The agreement is indicative of the weak-coupling limit and of adequate statistical sampling for the MD. In principle, the EOS parameters including temperature corrections may be calculated from these numerical results and the analytic form of the potentials. The predicted static thermodynamic properties will be very

Table 1
Thermodynamic parameters for equilibrium hydrogen plasma from MD, $x_\alpha = 1/2$, $q_p = -q_e = 1$. All results exclude the correction terms of $\langle\partial V/\partial T\rangle$ and $\langle\partial^2 V/\partial T^2\rangle$ in Eqs. (23) and (26). Density ρ is in units of 10^{25}/cc, temperature T is in keV. Extensive quantities are expressed per hydrogen atom. The HNC compressibility is obtained from the direct correlation functions and [21], Eq. 10.2.25.

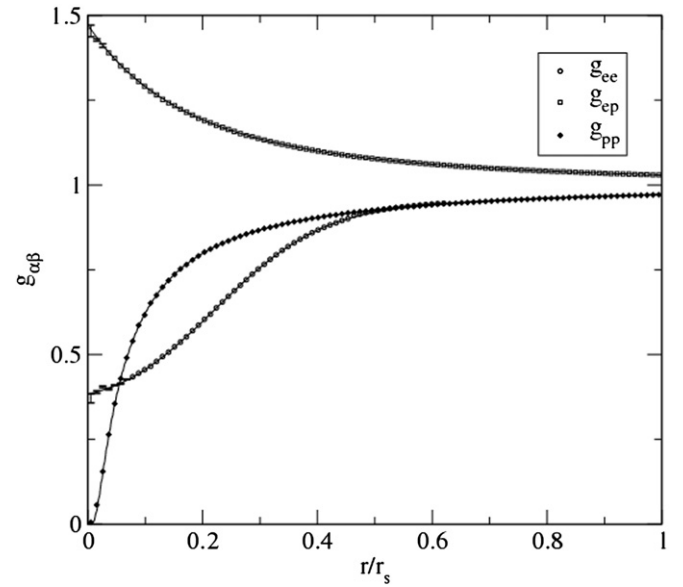| ρ	T	$\Delta\Phi$ (HNC)	$\Delta\Phi$ (MD)	c_V(MD)	$[1/\rho T\chi_T - 1]$(HNC)
0.125	0.25	−0.03255	−0.03288(1)	0.0164	−0.009856
1.0	0.50	−0.02666	−0.02665(1)	0.0166	0.002658
1.0	1.00	−0.01028	−0.01028(1)	0.00668	0.0001575
8.0	2.00	−0.00506	−0.00504(1)	0.00779	0.01215

Fig. 5. Pair distribution functions for hydrogen at a density of 10^{25}/cc and temperature of 1 keV using the Dunn-Broyles and Deutsch potentials [20]. The black curves show the HNC functions; the symbols show the related MD results. Explicit error bars are shown at small r, where they are larger than the symbol sizes.

similar as well, since they are simply given by averages over these functions.

5.2. Temperature relaxation

The electron–ion temperature equilibration rate is important in ICF research because thermonuclear burn in capsules containing DT plus high-Z dopants is expected to take place at least partly out of equilibrium [1]. In order to better understand temperature equilibration in general, we have used our MD capability with different statistical potentials to compute the electron–ion relaxation time, τ_{ei}, for two plasmas: fully-ionized hydrogen, and a fully ionized hydrogen plasma doped with 10 atomic percent Ar^{+18}. For simplicity we consider temperature equilibration only in the absence of radiation.

The legacy theoretical result for τ_{ei} is the Landau–Spitzer (LS) relaxation rate [5],

$$\frac{1}{\tau_{ei}} = \frac{8\sqrt{2\pi}\rho_i Z_i^2 e^4}{3m_e m_i c^3}\left[\frac{T_e}{m_e c^2} + \frac{T_i}{m_i c^2}\right]^{-3/2}\ln\lambda_{ei}, \quad (33)$$

where $1/\tau_{ei}$ is the rate at which the electron temperature, T_e, changes given an ion temperature, T_i, according to (assuming a single species of ions),

$$\frac{dT_e}{dt} = \frac{T_i - T_e}{\tau_{ei}}. \quad (34)$$

Here, m_e and m_i are electron and ion masses, Z_i is the ion charge, T_e and T_i are electron and ion temperatures, and ρ_e and ρ_i are the number densities. The ln λ_{ei} factor is the so-called Coulomb logarithm, equal to the logarithm of the ratio of maximum to minimum impact parameters in an effective two-body scattering event, ln (b_{max}/b_{min}). In LS, b_{max} is taken to be a Debye screening length, and b_{min} is set equal to the maximum of $(\lambdabar_e, b_0)$, where $\lambdabar_e$ is the electron thermal de Broglie wavelength and b_0 is the classical distance of closest approach (also called the Landau length) which roughly equals $Z_i e^2/T_e$. Other more modern theories for τ_{ei} exist as well [56,57]; all predict relaxation rates which are similar to LS (as long

as the temperatures are high enough for the individual species statistics to be classical), but with slightly different choices of $\ln\lambda_{ei}$. We can use MD simulations to differentiate between these candidate theories, as well as to study physics which is beyond the realm of weak plasma coupling, where LS and related approaches apply [57–59].

Simulations for these two-temperature problems are initialized by first placing the particles on a regular interpenetrating lattice, imparting random velocities from two-temperature Maxwell–Boltzmann distributions, and then propagating them with individual Langevin thermostats at the species temperatures. In order to rid the simulations of unphysical initial correlations (such as those imposed at the very outset), the system is allowed to evolve with the masses of the different species set to be nearly equal (so the resulting equilibration is fast). After this initial equilibration, the masses and velocities are adjusted, and the thermostat is re-applied. Relaxation is allowed to happen again though some aspects are slower now with more disparate masses. This process is repeated several times until no transient behavior is evident, at which point the system with its desired mass ratios and initial species temperatures is allowed to evolve microcanonically.

Time-steps for the MD are small, consistent with the fast electron motion and the steepness of Coulomb-like potentials at the short ranges probed in the closest encounters. For the τ_{ei} studies with the quantum statistical potentials, we find that time-steps in the range of 10^{-4}–10^{-5} fs are sufficient [59–61].

In some cases, particularly ones in which one or more high-Z element is considered, we find it beneficial to use scaled ion masses: $m_{scaled} = \alpha \cdot m_{physical}$, where $\alpha < 1$. This reduces the total simulation time since more similarly massed species relax faster. If we assume that this is a simple kinematic effect, the physical answer can then be recovered by multiplying the resulting simulation time by $1/\alpha$ (see the prefactor in Eq. (33)). However, one must be careful: changing the relative masses of the equilibrating species can alter the extent to which each individual species participates in screening the interparticle interactions at large distance. This can then affect the b_{max} within the Coulomb logarithm. For instance, in a hydrogen plasma, the protons respond too slowly to screen the e–p interaction in any meaningful way during temperature equilibration [57]. But in an electron–positron plasma, both species would participate equally in the screening. The figure of merit here is the ratio of ion to electron plasma frequencies. Since this is proportional to $Z_i\sqrt{m_e\rho_i/m_i\rho_e}$, one must be especially cautious when Z_i is large, since then the scaled-mass ion can easily have a plasma frequency which approaches that of the electrons when it would not otherwise do so for the physical mass ratio.

5.2.1. Hydrogen plasma

Fig. 6 shows the absolute value of the initial ($t = 0$) slope of the electron temperature, dT_e/dt, as a function of $T_e(t = 0)$, for 2-temperature H simulations along the $\rho = 10^{25}$ 1/cc isochore. For each case, we choose $T_p(t=0) = 0.8T_e(t=0)$. Magenta squares are the MD results as computed with the Dunn–Broyles statistical potentials [20], and with 512,000 electrons and 512,000 protons in each simulation cell. The maximum in dT_e/dt at $T_e \sim 1$ keV comes from the fact that $dT_e/dt \propto T_p - T_e \propto T_e$, together with: $b_{max} \sim \lambda_{Debye} \propto T_e$, $b_{min} \sim \lambdabar_e \propto 1/\sqrt{T_e}$, and the T_e-dependence of the LS-prefactor in Eq. (33) (note that at these temperatures and for $Z_i = 1$, $\lambdabar_e > b_0$, so $b_{min} = \lambdabar_e$ is appropriate). All other symbols indicate the results [61] of various versions of the generalized Lenard–Balescu (GLB) approach presented in Ref. [57]. In GLB, plasma screening and quantum diffraction are explicitly taken into account, so the *effective* Coulomb logarithm is determined without the need for *ad hoc* cutoffs, as in LS. The connected red symbols show the results of the quantum version of GLB with the inter-particle interactions taken to be pure
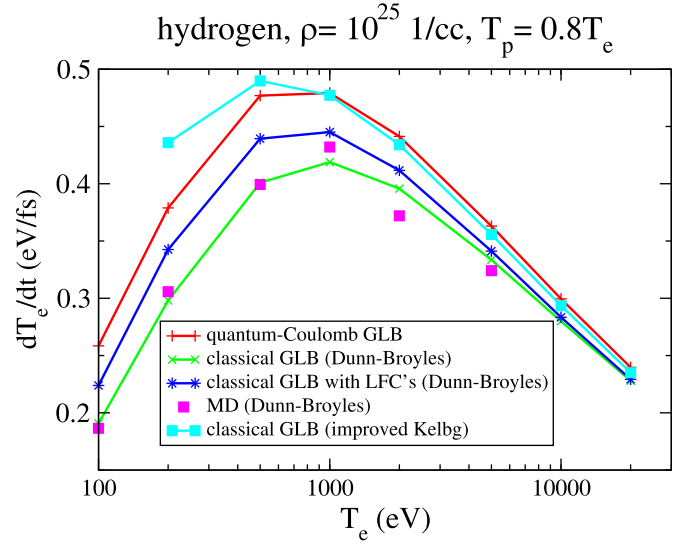

Fig. 6. dT_e/dt for H along an isochore at a density, $\rho = 10^{25}$ 1/cc. MD results (magenta symbols) and result from generalized Lenard–Balescu calculations of various types are also presented (see text). The electron-ion coupling is $\Gamma_{ei} = 50\,\mathrm{eV}/T < 1$.

Coulomb, and with static local field corrections (LFC's) to the plasma's polarization set equal to zero [61]. This should be the correct answer at sufficiently weak coupling, and we note that it agrees extremely well with the quantum limit of another modern theory, BPS [56].

Though the MD results approach the quantum–Coulomb GLB predictions at high-T_e, they are systematically below them at all temperatures. We have seen this for other densities as well. The reason for this can be understood by considering the classical ($\hbar \to 0$) version of GLB where the Coulomb potentials are replaced by the Dunn–Broyles potentials. The results of this calculation (again, setting LFC's = 0) are indicated by the connected green symbols. These are in far better agreement with the MD. Thus, we see that for this problem, classical MD with statistical potentials has its limits: The replacement of the pure Coulomb interaction by the Dunn–Broyles potential, together with the use of classical rather than quantum dynamics, reduces dT_e/dt by roughly 10–15 % in this regime. This largely explains the lower effective $\ln\lambda_{ei}$'s we saw in MD results with Dunn–Broyles, in comparison to various theoretical approaches, in an earlier work on H plasmas [59]. Though the softening of the statistical potentials at short distance is meant to account for the salient features of quantum diffraction in a classical simulation, the true time-dependent quantum problem is different, of course. Still, it is encouraging that as T_e is increased, quantum–Coulomb and statistical potential GLB results approach each other, indicating that MD of this sort should actually yield the proper results for τ_{ei} in the limit of weak-coupling.

One somewhat surprising conclusion to be drawn from the results of Fig. 6 is that the approximation of *static* LFC's is likely a worse approximation than simply setting the LFC's equal to zero. The connected blue symbols represent the results of $\hbar \to 0$ GLB with static LFC's derived from the Hypernetted Chain (HNC) approximation with these same Dunn–Broyles potentials [61]. These are significantly further from the MD results than are the classical GLB results with LFC's = 0 (green symbols). It is not clear yet as to why this is the case, nor is it known if this is also true for quantum plasmas, where bona fide quantum diffraction is taking place.

The improved statistical potentials of the modified-Kelbg variety, introduced in Section 3, produce results for τ_{ei} which are considerably more in line with our expectations for the pure-Coulomb quantum case, at least at weak coupling. The connected

sky-blue symbols in Fig. 6 show classical GLB results using these potentials. Preliminary MD calculations with these potentials indicate similar answers. Above $T_e = 500$ eV (below this, the use of a statistical potential derived from a *pair* density matrix, as reported in Sections 3.1,3.2, is of questionable validity), these results are in strikingly good agreement with quantum pure-Coulomb GLB. This suggests that classical MD performed with the modified-Kelbg potential should be considerably closer to the quantum result than MD using the Dunn–Broyles form. We therefore learn that constructing statistical potentials by optimizing agreement with known *static* properties can produce more accurate results for *time-dependent* properties as well, at least in these weakly-coupled cases where we expect GLB to be accurate for these properties.

At stronger couplings, the differences between MD results for H using various statistical potentials can be smaller than the differences between candidate theories of τ_{ei}, such as LS, BPS, and other many-body theoretical approaches [62]. Here, MD with statistical potentials can be a powerful tool, though we must be cautious in using it in situations where the coupling is strong enough so that the spurious appearance of classical bound states may poison the result. We refer the reader to Ref. [59] for a discussion of stronger coupling in H, and the use of classical MD to discriminate between various models for $ln\lambda_{ei}$ (see in particular Fig. 2 of that work).

5.2.2. Ar-doped hydrogen plasma

We next consider a plasma consisting of hydrogen admixed with ten atomic percent fully ionized argon. The H density is taken to be $\rho_H \equiv \rho_p = 10^{25}$ 1/cc, so the Ar^{+18} and electron densities are $\rho_{Ar} = 10^{24}$ 1/cc and $\rho_e = 2.8 \times 10^{25}$ 1/cc. The simulation cell contains 560,000 electrons, 200,000 protons, and 20000 Ar ions. The initial temperatures are chosen to be $T_e = 4.46$ keV, and $T_p = T_{Ar} = 6.61$ keV. In these conditions, the Ar would indeed be fully stripped, so we neglect the complication of bound states in this study. Mass-scaling for the Ar and p ions is used: $\alpha = \alpha_{Ar} = \alpha_p = 0.01$; in the discussion that follows, we consider this system *without* rescaling the results to correspond to the associated $\alpha = 1$ values.

Fig. 7 shows MD results for the time-dependent temperatures of this system using the Dunn–Broyles potentials. We remind the reader that the results for the physical ($\alpha = 1$) system would correspond to dividing the time scale by α. Note first that the relaxation is highly asymmetric; the final equilibrated temperature

(mass-scaled!) Ar-doped H: $n_H = 10^{25}$ 1/cc, $n_{Ar} = 10^{24}$ 1/cc

Legend:
- p^+ (m= $0.01m_p$)
- Ar^{+18} (m= $0.01m_{Ar}$)
- e^-
- LS

Fig. 7. Time-dependent temperatures of the (mass-scaled!) Ar-doped H plasma (see text) as computed by MD with the Dunn-Broyles potentials. Also plotted are the results of Landau-Spitzer with judiciously chosen Coulomb-logarithms.

is far closer to $T_e(t = 0)$ than to $T_p(t = 0) \equiv T_{Ar}(t = 0)$. This is simply because the heat capacity of the electron subsystem is much larger than the heat capacities of the ions, since ρ_e is quite a bit bigger than ρ_p and ρ_{Ar}. Note next that even though we have chosen $T_{Ar} = T_p$ initially, the Ar and proton temperatures quickly separate. This is because: (1) m_{Ar} is quite a bit larger than m_p ($m_{Ar} = 39.6m_p$), and 2) the e−Ar energy transfer rate, per collision, is quite a bit higher than the e−p transfer rate, since $Z_{Ar} \gg 1$. Finally, notice that the resulting equilibrated temperature is slightly higher than that predicted by LS, also shown in Fig. 7. Since LS and all related approaches conserve *kinetic* (rather than total!) energy, this indicates the effects of time-varying *potential* energy in the simulations.

This potential energy effect can be understood as follows: Since $Z_{Ar} = 18$, the Ar−Ar coupling is rather high (even though $\rho_{Ar} = 0.1\rho_p$). Thus, the screened Ar subsystem possesses a sizable Coulombic potential energy, particularly when the ions are cold. In this simulation, the Ar start hot, so the Ar−Ar positional correlations are less important and the resulting potential energy is high (as in, less negative). At the end of the relaxation, when the Ar temperature has been driven down to just above the initial electron temperature, the Ar−Ar positional correlations are more pronounced and the plasma lowers its potential energy. Since total energy is conserved, the decrease in potential energy with simulation time t is exactly balanced by an increase in kinetic energy. This is then manifested in the rise in the final values of (T_e, T_p, T_{Ar}), as compared to LS and other theories which have no explicit potential energy contributions. This effect has been predicted [63] and recently derived in a rigorous fashion from many-body theory [64]. Modeling of this system using these and related theoretical methods is underway [61]. We also refer the reader to a recent MD study in which this effect was seen in an idealization of an SF_6 plasma [60].

The thin lines in Fig. 7 show results from LS for this plasma, where we have chosen the arguments of λ_{ep}, λ_{eAr}, and λ_{pAr} by appealing to physical intuition. At these temperatures, the electron de Broglie wavelength is considerably larger than the e−p Landau length. Thus we take $b_{min}(e, p) = \lambdabar_e$. Since $\lambdabar_e$ is comparable to the e−Ar Landau length, we again choose $b_{min}(e, Ar) = \lambdabar_e$, though we note that LFC's resulting from strong e−Ar correlations (and going beyond a simple LS picture) could be relevant here. For b_{min} (p,Ar), we take the corresponding p−Ar Landau length since this is considerably greater than the proton de Broglie wavelength.

The choices for b_{max} are a bit more difficult. For e−p, the choice of $b_{max} =$ electron Debye length is clear; we know that this is the proper choice for pure H [57], and the plasma frequency of the Ar ions is similar to that of the protons (since $\omega_p \propto Z/\sqrt{m}$), so their response time should also be slow enough to prevent their participation in screening the e−p interaction during the duration of a typical scattering event. For p−Ar, we choose $b_{max} =$ total Debye length, since the very fast electrons will surely respond and screen and the only slightly more sluggish p and Ar may as well (for our choice of ρ_{Ar} and α, p and Ar plasma frequencies are very similar, and each is 7−8 times lower than the electron plasma frequency). For $b_{max}(e,Ar)$, we again choose the electron Debye length, since the e−Ar interaction time is set primarily by the fast electron motion. The comparisons in Fig. 7 suggest that these choices are reasonable. Note, however, that LS invokes the static screening hypothesis; for each pair of species, we are forced to choose the best *static* screening length for b_{max}. GLB calculations for this system, in which the self-consistent *dynamical* screening of the coupled 3-species plasma is considered, are currently underway [61]. It bears repeating, however, that even this approach, by itself, will not account for the potential energy-driven shift in the final equilibrated temperature mentioned above.

In general, temperature equilibration in plasmas consisting of H (or DT) + high-Z dopants will have the features seen here: asymmetric relaxation due to $\rho_e > \rho_i$, and shifts in the equilibrated
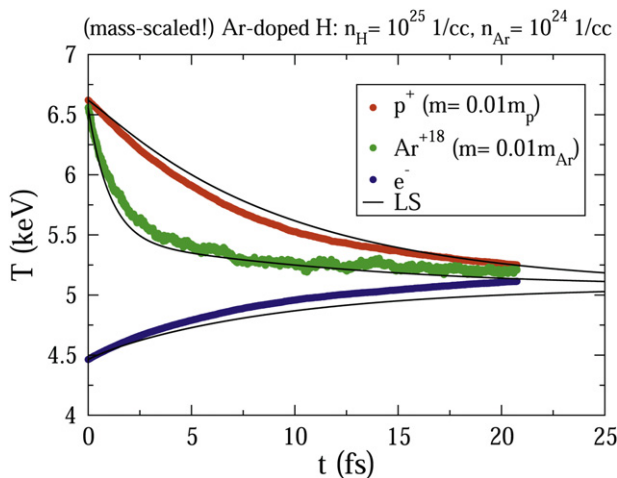
temperature due to potential energy resulting from large Z–Z coupling. Our results for pure H show us how well we should expect to predict the true quantum result for the e−p channel of the energy transfer using classical MD with various statistical potentials. MD of this type performed on both pure H and H + higher-Z dopants allows us to include many-body correlations that may be particularly important when the Z–Z coupling is high. In any real plasma of this type, however, one must deal with the problem of time-dependent ionization in the high-Z ion, since many ions will not be fully stripped throughout the course of the equilibration. This is an active research area we are currently pursuing.

5.3. Dynamic structure factor and energy transport

The dynamic structure factor for a homogeneous, stationary system,

$$S_{\alpha\beta}(\mathbf{k}, \omega) = \frac{1}{N} \int dt e^{i\omega t} \int d\mathbf{r} e^{-i\mathbf{k}\cdot\mathbf{r}} \langle \delta\rho_\alpha(\mathbf{r}, t) \delta\rho_\beta(0, 0) \rangle, \quad (35)$$

is the time-dependent generalization of Eq. (28). If the density fluctuations are Fourier transformed to $\delta\rho(\mathbf{k}, t)$, then by means of the convolution theorem (neglecting a constant term) one obtains

$$S_{\alpha\alpha}(\mathbf{k}, \omega) = \frac{1}{N} \int dt e^{i\omega t} \langle \delta\rho_\alpha(\mathbf{k}, t) \delta\rho_\alpha(-\mathbf{k}, 0) \rangle \quad (36)$$

Spectral features in $S(\mathbf{k}, \omega)$ reveal the excitation spectrum of the plasma. For example, the peak in Fig. 8 shows the electron plasma excitation for a hydrogen plasma with $\rho = 10^{25}$/cc and $T = 10$ keV. The $k = 0$ limit corresponds to $\omega_p = \sqrt{4\pi\rho_e q_e^2/m_e} = 178$ fs^{-1}. (This run used mass scaling, $m_p = 100*m_e$, in order to make the ion-acoustic wave period more commensurate with the duration of the run.)

Eq. (36) applies to equilibrium situations, where the expected correlation function is not time-dependent. In explicitly non-equilibrium problems (such as slow temperature relaxation), it can be useful to filter the time series so that the Fourier transform is restricted to a finite time interval. For example, the time series in the integrand of Eq. (35) can be multiplied by a low-pass Gaussian filter centered at time t' before applying the frequency transform. This provides an estimate of the evolving correlation function at time t' that can be compared to analytic predictions, as employed in

Sec. 5.2.2. The time-resolved behavior of the $\rho = 10^{25}$/cc and $T = 1$ keV equilibrium plasma is shown in Fig. 9, using a Gaussian with a width of 3.3 radians/fs. The time-integration of this quantity would approximate to the results of Fig. 8. Time-dependent analyses of this sort will be used in future studies.

Spectral properties of $S(\mathbf{k}, \omega)$ determine the energy transfer rates between charged particles of different species. Density fluctuations in subsystems of ions and electrons are coupled by the Coulomb interaction and systematically transfer energy when they are resonant in k and ω. The fluctuation−dissipation theorem relates the structure factor and the spontaneous thermal fluctuations to the spectral representation of the density response, Im($\chi(k, \omega)$) or Im($\varepsilon^{-1}(k, \omega)$) for each of the subsystems. The overall energy transfer rate is governed by the product of these quantities, integrated over k and ω.

Microscopically, the stopping power, dE/dx, of a charged projectile in a plasma depends on the instantaneous force on the projectile from electrons and ions, due to the electric field from the charge density response induced by the moving projectile ([65], Eq. (39)):

$$\frac{dE}{dx} = \frac{Z^2 e^2}{(2\pi)^3} \int d\mathbf{k} \frac{\mathbf{k}\cdot\mathbf{v}}{k^2} \text{Im}\left[\frac{1}{\varepsilon(\mathbf{k}, \mathbf{k}\cdot\mathbf{v})}\right]. \quad (37)$$

Equivalently in a particle picture, $dE_k(t)/dt = \mathbf{v}_{proj}\cdot\mathbf{F}_{proj}$ in term of the velocity $\mathbf{v}_{proj}$ of the projectile and the force $\mathbf{F}_{proj}$ acting on it. In practice, the direct MD approach for the total stopping power is to explicitly record the projectile kinetic energy, $E_k(t)$, and trajectory, $x(t)$; it is then straightforward to derive $dE(x)/dx$.

$S(\mathbf{k}, \omega)$ also determines the elastic and inelastic scattering rate, R, of, e.g., an incident photon or particle beam ([65], Eq. (40)),

$$R(\mathbf{k}, \omega(k)) = \frac{1}{\hbar^2} |V(\mathbf{k})|^2 S(\mathbf{k}, \omega(k)), \quad (38)$$

where $\omega(k)=\mathbf{k}\cdot\mathbf{v}$ and $V(\mathbf{k})$ is, e.g., the Coulomb interaction. The processes represented by Eqs. (37) and (38) are central to the validation experiments discussed in Section 6. Note that the symmetry of the response function implies this symmetry of the dynamic structure factor

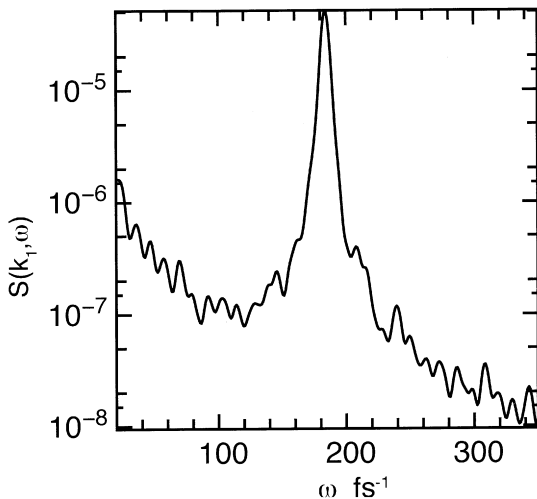$$S_{\alpha\beta}(-\mathbf{k}, -\omega) = e^{-\hbar\omega/T} S_{\beta\alpha}(\mathbf{k}, \omega), \quad (39)$$

Fig. 8. Dynamic structure factor versus frequency for $k/k_D = 0.126$ in a hydrogen plasma at $\rho = 10^{25}$ /cc and $T = 1$ keV.
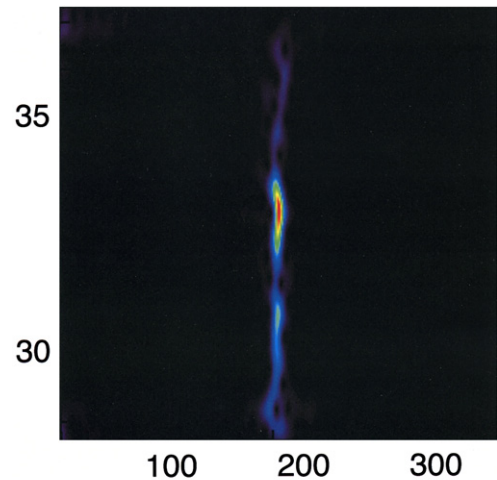

Fig. 9. Time-resolved dynamic structure factor shows energy fluctuations in the long-wavelength plasma oscillation. x-axis: frequency ω in fs^{-1}; y-axis: time in fs from an arbitrary origin.

which comes into play in interpreting x-ray Thomson scattering spectra as in Section 5.3.2; Eq. (39) is an expression of detailed balance.

5.3.1. Charged-particle stopping

Fig. 10 shows dE/dx versus velocity for a single $Z = -10$ projectile with the mass of a neon nucleus in a one component electron plasma at strong coupling, $\Gamma_{ee} = 10$. A statistical potential is not used as there are no classical bound states for the repulsive interactions; instead the simulation is performed for a pure Coulomb interaction. The MD consists of 128,000 particles in a cubic cell of $L = 1075$ Å. The projectile trajectory is angled within the box to avoid overlapping the wake field from adjacent, periodic replicas of the central projectile. A Langevin thermostat with 60 fs time constant is applied to the electrons to keep the temperature steady. Projectile simulations are initialized for 100 fs to allow any transients to decay; the full simulations are 400 fs in duration. The projectile kinetic energy typically changes by a few percent over the entire simulation. Stopping values are computed from the energy difference at 100 fs intervals. The solid points and error bars show the mean stopping and standard deviations from the three samplings.

The stopping behavior shows the expected trends versus v_{proj}/v_{th}. In the slow projectile limit, dE/dx is linear in v, analogous to a viscous drag term in Brownian motion ([65], Eq. (42)). The analytic Bohr result for the OCP,

$$\frac{dE}{dx} = \left(\frac{Z_{proj}e\omega_p}{v_{proj}}\right)^2 \ln\left(\frac{mv_{proj}^3}{Z_{proj}e^2\omega_p}\right), \tag{40}$$

is a linearized dielectric model that applies in the high velocity limit. Fig. 10 also shows the results for other analytic models [66]: Bohr with the Chandrasekhar correction, and with an additional correction due to Peter and Meyer-ter-Vehn. These approximations tend to overestimate the peak in dE/dx. Better agreement can be obtained by accounting for multiple scattering processes [67].

A characteristic wake field is shown in Fig. 11, for the same parameters as in Fig. 10. v_{proj}/v_{th} lies near the peak in dE/dx in Fig. 10. There is a faint artifact in the density response along the central axis preceding the projectile. The density is time- and cylindrically-averaged to reduce noise, but this axis is averaged over
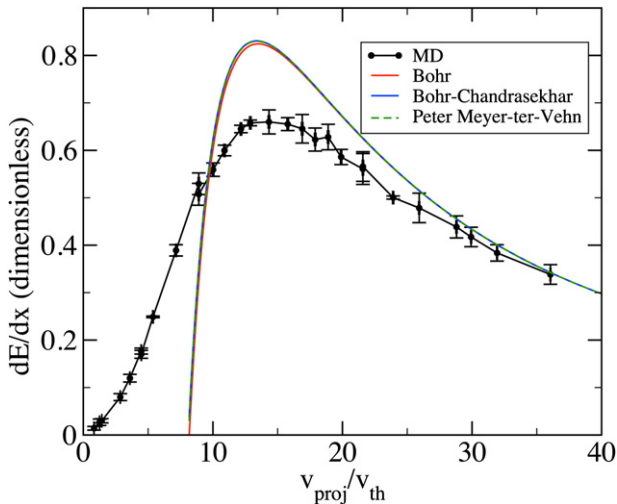

Fig. 11. OCP wake field due to a $Z = -10$ projectile ("anti-neon") in an electron gas with $\Gamma_{ee} = 10$. The projectile is centered in the upper third of the field of view, moving upwards. The density response is shown in grayscale with the wake trailing behind. The log of the energy transfer field, $\ln(\mathbf{F}\cdot\mathbf{j}_e)$ is shown in color, truncated at a small value.

Fig. 10. Stopping dE/dx versus projectile velocity from MD (solid symbols) and analytic models (curves) for a $Z = -10$ projectile in an electron gas of $\Gamma = 10$. The electron thermal velocity is $v_{th} = (kT/m_e)^{1/2} = 1.38$Å /fs. dE/dx is expressed in units of $\sqrt{3}\Gamma^{3/2}kT/\lambda_D = 2.466$ eV/ Å with $\lambda_D = 2.42$Å. The three models are indistinguishable for this case.
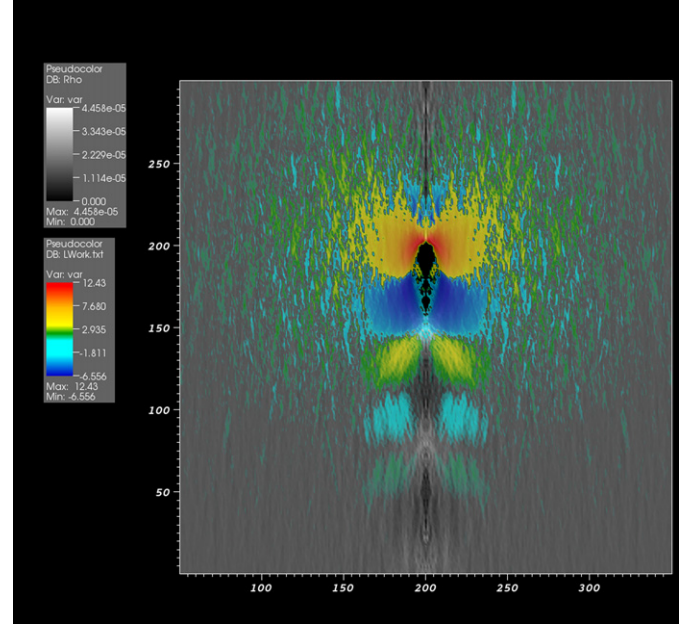
a comparatively small volume. The screening cloud surrounding the projectile is clearly visible in black; some plasma turbulence intrudes behind the projectile. The energy transfer for fast projectiles is dominated by a sharp peak immediately ahead of the projectile, which corresponds to the region of strong binary scattering. The magnitude of the energy transfer to the plasma falls off rapidly behind the projectile; the tail is made visible by the logarithmic scale. The transfer alternates in sign due to OCP collective oscillations. This highly peaked distribution is a consequence of the singular Coulomb interaction for this model with charges of the same sign. The usual statistical potential would soften the short range interaction to account for quantum diffraction over a thermal distribution. This thermal-average softening of non-equilibrium scattering would then underestimate the strong, short-range interaction and would distort both the predicted stopping and straggling.

A comparable dE/dx result is shown for a repulsive model of an alpha particle in Fig. 12. The OCP target is of the same density, but with $\Gamma_{ee} = 1$. These simulations are for 64,000 particles in a periodic system of $L = 853$ Å and a Langevin thermostat with a 100 fs time constant. The MD stopping for this lighter projectile and higher temperature shows a larger variance representative of the essentially stochastic particle scattering. Most of the variability in the energy loss is due to collisions at small impact parameters. Over long times compared to the characteristic rate of small impact parameter collisions, the energy loss will have a normal distribution around the mean dE/dx. This reveals the so-called straggling that causes a monoenergetic beam to stop at a range of depths. Again, note that the effect of these collisions on both dE/dx and the straggling would be underestimated if QSPs were used.

In a neutral electron−ion plasma, there is a second peak in the stopping due to ion scattering. Like the electron peak, it will occur for a projectile velocity at a few times thermal velocities of the much slower target ions. This makes the energy split, or the percentage of energy deposited into electrons versus ions, strongly velocity dependent. The energy transport calculation shown in
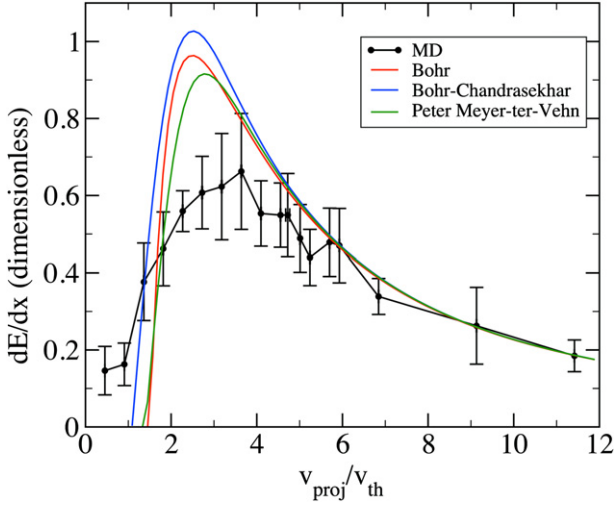
Fig. 12. Stopping dE/dx versus projectile velocity for a repulsive $Z = -2$ projectile ("anti-helium") in an electron gas with $\Gamma_{ee} = 1$. The electron thermal velocity is $v_{th} = (kT/m_e)^{1/2} = 1.38$Å /fs. dE/dx is expressed in units of $\sqrt{3}\Gamma^{3/2}kT/\lambda_D = 2.466$ eV/ Å with $\lambda_D = 2.42$Å.

Fig. 13. Comparison of energy loss models for carbon at 20 eV and 2.267 g/cm^3. Blue diamonds: ddcMD with frozen C^{2+} ions; green triangles: ddcMD with C^{6+} ions; black line: result from SRIM2008; red squares: ddcMD with C^{2+} plus a bound electron contribution (4/6 of SRIM result). (For interpretation of the references to colour in this figure legend, the reader is referred to the web version of this article.)

Fig. 11 can be repeated for the forces on the ions separate from the electrons. Thus the energy split can be quantified in regimes where classical MD is applicable, including strong-coupling situations.

However, stopping in partially ionized matter is complicated by the presence of bound core electrons; core dynamics are not strictly addressed by classical MD simulations with QSPs. Bound states are prevalent in warm dense plasmas, and they are expected even in hot, burning plasmas when there are high-Z impurities present. A complete simulation of a burning neutral plasma thus requires some quantum-corrected analog of a statistical potential to prevent singular binding of classical point charges plus an explicit treatment of bound electron degrees of freedom. Such improvements are already being explored.

In the meantime, the predictions from the standard classical MD model are of interest even before a complete capability for quantum bound states is in place. Warm dense carbon applications are particularly relevant, as there are particular experiments (see Section 6.1) to compare the simulations against. Two MD models for warm dense carbon are considered here in particular. The first is a C^{2+} model. The point ions in the simulation have the carbon mass but a charge of $+2$ to simulate the doubly-ionized atom. This model approximates the number of free electrons for the expected ionization of a carbon plasma at $T = 20$ eV (approximately 2.2 per carbon). Strictly, the free electrons are semi-degenerate for experiments at these temperatures, while the MD is restricted to a non-degenerate approximation. For fast projectiles, the proton-C potential is not of concern; most of the stopping is due to the proton–electron interaction. A more serious approximation is that the core electrons are held rigid and do not participate in screening or stopping at all. Accordingly, a classical C^{6+} model is also considered. This model uses the conventional C statistical potential at 20 eV, and it includes the core electrons as classical bound states. The reliability of the resulting $g_{Ce}(r)$ is not considered, nor is the lack of discrete energy levels for the bound states.

C^{2+} MD calculations are performed for 64,000 C^{2+} atoms at a density of 2.267 g/cm^3 at $T = 20$ eV; C^{6+} simulations are for 24,000 C atoms at the same density and temperature. The resulting proton stopping power is shown in Fig. 13 along with the results of an SRIM calculation [68]. (SRIM is Stopping and Range of Ions in Matter, a commercial software package.) Both MD calculations underestimate
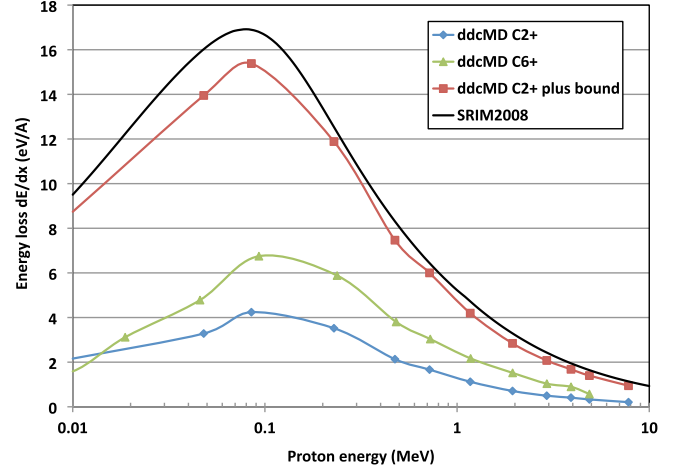
dE/dx as compared to the SRIM model. Much of the deficit can be attributed to the treatment of the core contribution to the overall stopping. If the Bethe−Bloch model is used for the bound electron contribution, then the MD C^{2+} stopping is in reasonable agreement, slightly below the SRIM model (see Fig. 13). The MD results are also affected by the use of the (softened) statistical potential for the electron−proton interaction. If the proton, electrons, and C^{2+} particles are all given the same sign and their scattering is treated with the Coulomb potential, the peak stopping of the C^{2+} curve is almost doubled in magnitude (not shown). Again, if the Bethe−Bloch bound state contribution is added, the resulting stopping power would be slightly higher than the SRIM model, still in reasonable agreement. As expected, the presence of quantum bound electrons requires a careful account of their dynamic response functions and of the effective potentials that couple the particles in the system.

5.3.2. Scattering of a probe beam

The essence of a photon−plasma scattering experiment is that a probe beam characterized by $\mathbf{k}_1$ and ω_1 is scattered into a beam $\mathbf{k}_2$ and ω_2 with a differential cross section [69,70]

$$\frac{d\sigma}{d\Omega d\omega_2} \propto S_{ee}(\mathbf{k}_1 - \mathbf{k}_2, \omega_1 - \omega_2). \tag{41}$$

At a given scattering angle θ, the magnitude k of $\mathbf{k}_2 - \mathbf{k}_1$ is approximately $k = 2k_1 \sin(\theta/2)$ since the frequency shift is $\ll \omega$. The spectrum of scattered radiation in a fixed direction arises from the ω-dependence of $S_{ee}(k,\omega)$, and shows resonant features associated with Langmuir (plasmon) waves and ion-acoustic waves. The asymmetry with respect to $\omega_2 > \omega_1$ versus $\omega_2 < \omega_1$ that can be derived from Eq. (39) allows one to infer the electron temperature [71]. The frequency positions of the resonances gives information about the electron density (from ω_{pe}) and the ion temperature (from the ion-acoustic frequency). The frequency-integrated intensity scattered in a particular direction is given by

$$I \propto \frac{d\sigma}{d\Omega} \propto S_{ee}(k), \tag{42}$$

so the angular distribution conveys information about the static structure factor. For a crystalline sample, the angular distribution is multiplied by the factor $|\sum_{ion} \exp(i\mathbf{k} \cdot \mathbf{r}_{ion})|^2$ expressing the ion–ion

correlations, which limits the scattering essentially to those directions satisfying the Bragg condition. In this case it is the relative intensities of the different Bragg reflections that contain $S_{ee}(k)$ information. When and if the crystal melts, then the intensity peaks at the Bragg angles are broadened and diminished.

6. Experiments and validation

The experimental validation of our computational Molecular−Dynamics/Monte Carlo capability is significantly complicated by the limited phase-space regime that is accessible to both simulations and experiments. The experimental preparation of a well-characterized high-density plasma state continues to be challenging. Different methods have been proposed to excite solid-density materials, including heating by laser [72] and particle beams [73,74]. One of the main issues is the evolution of the material during the heating process, which can lead to ill-defined states of matter. In the Cimarron project, we have used two different approaches in parallel to heat and probe solid-density matter: intense, ultra-short pulses of X-rays from the Linac Coherent Light Source (LCLS), and proton beams generated from thin foils irradiated with intense, ultra-short optical laser pulses at the Jupiter Laser Facility (JLF). Both of these approaches allow one to heat micron-sized samples to temperatures greater than 10 eV sufficiently rapidly that the density remains that of the cold solid.

6.1. JLF experiment

The goal of this experiment was to measure the energy loss, dE/dx, of protons propagating through material heated to warm dense matter (WDM) conditions, which is to say, a solid in which the temperature is comparable with or somewhat higher than the Fermi temperature. For normal density carbon, this means a temperature around 20 eV. For energetic ions, the energy loss of the projectile is dominated by collisions with electrons in the target [68]. In our experiment, the target was polycrystalline graphite. At WMD conditions, the carbon atoms are partially ionized, so that both the remaining bound electrons and the free, plasma electrons contribute to the energy loss of the protons moving through the target. Since the degree of ionization depends on the temperature, the relative contributions of the bound and free electrons also change with temperature. In addition, the total energy loss of a proton with a given incident energy depends strongly on the areal density of the target. Therefore, in a stopping experiment with a plasma target, one needs to characterize the temperature, density and thickness of the plasma and use a technique that minimizes spatial and temporal gradients. In addition, one needs to measure the energy distribution of both the incident and the transmitted ions to be able to infer dE/dx.

In view of these requirements, we chose a "pump-probe" technique for our initial experiment [75], sketched in Fig. 14. We used an intense, energetic proton beam to heat a micron-sized solid target, and then sent a second, independent proton beam through the heated target. Both proton beams were generated by irradiating thin metal foils with intense, 2 ps-long pulses from the Titan laser at the JLF in Livermore. It has been well established over the last decade that such irradiation produces energetic, highly collimated ion beams that propagate perpendicular to the rear surface of the irradiated foils [76]. The protons are accelerated from a very thin, hydrogen-containing contaminant layer on the surface of the foils. Furthermore, the ions are accelerated to their asymptotic velocities in less than 10 ps when the laser pulse duration is in the range 0.1−5 ps. This allows for rapid, volumetric heating of solid samples. In our experiment, the distance between the proton source and the heated carbon target was only 200 μm to maximize the proton
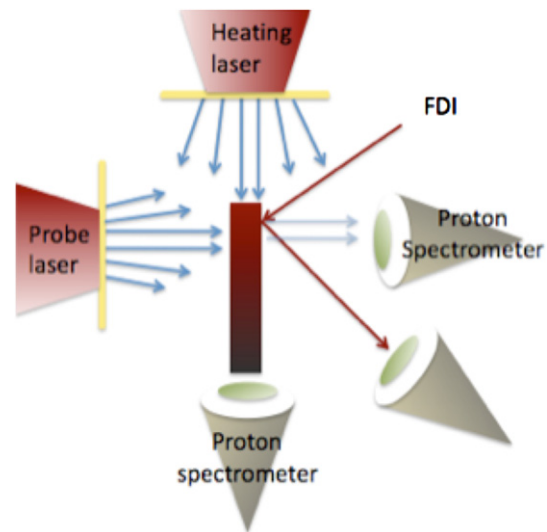

Fig. 14. Schematic of the proton energy loss experiment. The blue arrows depict the two proton beams. The reddish rectangle represents the carbon target. FDI is the interferometric diagnostic used to measure the surface expansion velocity of the heated target. (For interpretation of the references to colour in this figure legend, the reader is referred to the web version of this article.)

fluence on the target (hence the resulting temperature) and to minimize the temporal spreading of the short-duration proton beam due to time-of-flight (hence the heating time).

The temperature of the heated carbon sample, about 13 eV, was inferred from a measurement of the expansion velocity of the target surface. We used time- and space-resolved interferometry (TASRI) to measure the surface velocity [77,78]. The temperature extracted from the TASRI data was consistent with the results of 1D hydrodynamic simulations of the proton-heated carbon target. These simulations used as input the known target geometry, and the energy distribution and divergence of the heating proton beam, which we measured on separate laser shots. The simulations showed that the temperature of the heated sample reached 14 eV in about 15 ps, and then remained approximately constant for 80 ps. During this time, there was minimal expansion of the target, so that it remained at its original, solid density.

The proton beam used to probe the heated carbon sample was generated by irradiating a separate 25 μm Au foil with a second 2 ps-long laser pulse. The relative timing of the two laser pulses was adjusted so that the probe proton beam passed through the carbon target while it was at the maximum temperature. We measured the energy distribution of the incident and transmitted protons using a recently developed, novel magnetic spectrometer [79]. In the experiments reported here [75], we obtained the incident and transmitted proton spectra on different laser shots, which means that shot-to-shot variation was a major source of error for the inferred value of dE/dx. We recorded energy spectra of the protons, which passed through the heated carbon target, for a range of thicknesses between 2.5 and 17 μm. Fig. 15 shows examples of the incident and transmitted proton spectra. A simple comparison of the peak positions in the two spectra gave 84 ± 20 eV/nm as an estimate of dE/dx at a projectile energy of 500 keV. For comparison, the value for cold polycrystalline graphite, with a density of 1.7 g/cm^3, is 60 eV/nm [68].

Simple ionization models suggest that the degree of ionization of carbon at 15 eV is roughly $Z = 2.2$. A ddcMD calculation of proton stopping in a 20 eV C plasma with two free electrons (but no bound electrons, just a structureless C^{+2} ion) gave 21 eV/nm at 475 keV, a value about four times smaller than the experimental estimate.
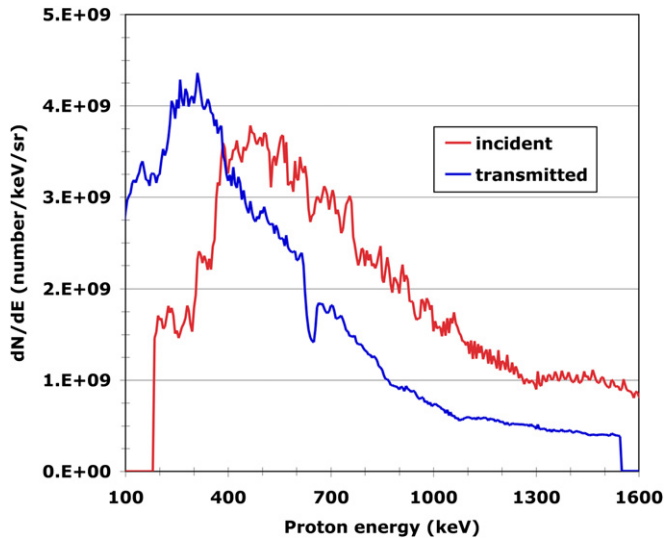
Fig. 15. Spectra of the incident (red) and transmitted (blue) protons obtained with the magnetic ion spectrometer. The target was a 2.5 μm thick polycrystalline graphite foil, which was volumetrically heated by another proton beam. The two spectra were recorded on different laser shots. (For interpretation of the references to colour in this figure legend, the reader is referred to the web version of this article.)

Fig. 16. Bragg diffraction peak of graphite excited by the LCLS pulse.

This strongly suggests that the contribution of the bound electrons to the stopping at WDM conditions is important. Indeed, as discussed in connection with Fig. 13, adding a bound electron contribution, calculated with the Bethe–Bloch model [68] for these conditions, to the ddcMD result gave 85 eV/nm, which is close to the experimental estimate. Clearly, simulation models must include a treatment of the bound electrons and their contribution to ion stopping in partially ionized plasmas. This improvement is in progress.

6.2. LCLS experiment

Particularly useful to excite solids are X-ray beams, since they penetrate solid-density materials and their absorption properties are relatively well understood. Short duration X-ray pulses offer the additional advantage that the material does not undergo macroscopic changes during the heating process. Therefore, short-pulse X-ray beams can be used to generate uniform, dense plasmas of known energy density.

At the same time, owing to their large penetrating power, X-ray beams can also be used to characterize dense plasmas through X-ray scattering. Until recently, X-ray sources have not been sufficiently bright for this application. Recently, a major breakthrough has been achieved with the advent of X-ray free-electron lasers (XFELs), that provide sub-100 fs X-ray pulses between 500 eV and 10 keV with pulse energies in excess of 3 mJ. These pulses can be focused to a diameter of 1 μm and smaller. The first EUV free electron lasers became operational at DESY in Hamburg, Germany in 2003 [80]. The Linac Coherent Light Source (LCLS) is the first XFEL that has produced X-ray pulses up to 10 keV since 2009 [81]. We recently used the highly penetrating, ultra-short, high-intensity LCLS radiation to isochorically excite solid-density graphite into the WDM regime, hot enough that we can simulate the experiment. During the heating pulse the sample reached a solid density, strongly coupled plasma state. We then probed the sample using Bragg and Thomson scattering from the same X-ray radiation, providing information about the ultrafast dynamics of the graphite electron and ion system. An extensive set of data with varying pulse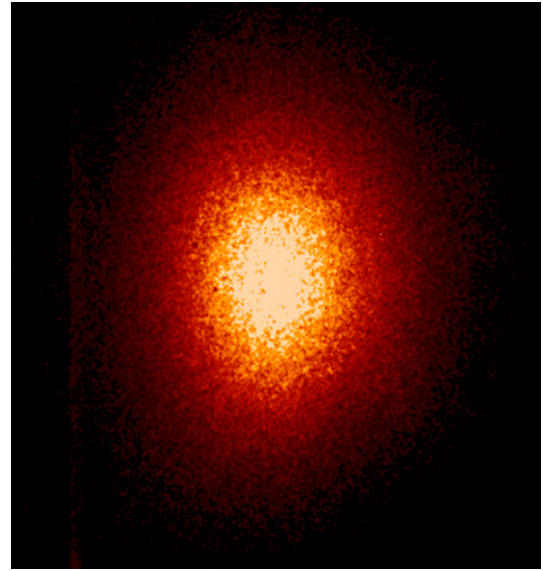 length and fluence were collected. Fig. 16 shows the Bragg reflection from single-crystal graphite, which can be used to characterize the materials dynamics. The Bragg peak intensity is strongly dependent on the atomic order and ionization state of the ions. Fig. 17 shows simulation results of the lattice dynamics for a 70 fs-long pulse, for pulse parameter similar to the ones encountered in the experiment. The simulations suggests that initial atomic motion occurs within tens of fs, and that the graphite transforms into a plasma at the end of the pulse. This experiment constitutes the first X-ray characterization of X-ray-induced plasmas at sub-ps timescales. Analysis of this data is in progress.

7. New directions for MD simulations of plasmas

7.1. Motivations

Ideally, to simulate the hot dense plasmas discussed in this paper, we would like to solve the many-body time-dependent Schrödinger equation (TDSE). This is a practical impossibility so the traditional approach has been to rely on MD with QSPs. MD provides an accurate numerical solution to the many-body classical particle dynamics. It is a valuable tool for investigating the variety of complex non-equilibrium processes of hot dense matter [46,47,57,82]. It handles strongly coupled ions exactly and strongly coupled electrons depending on the form of the potential chosen. However, the method suffers from two serious drawbacks that need to be solved if this method is to be used reliably to inform us of the accuracy of theoretical treatments of hot dense matter. First, when used for non-equilibrium plasma simulations, QSPs may not be accurate. In other words, within the traditional MD framework, the fidelity to quantum mechanics is limited. Second, and perhaps more serious, is that explicit electron dynamics leads to a time step limitation that is a small fraction of the inverse of the electron plasma frequency, and this is too small to make simulating fusion plasmas feasible.

In this section we explore ideas for alternative treatments. The first of these is orbital-free density functional theory, in which ions are treated with classical MD and hence can be strongly coupled. This method works when electron dynamics may be ignored; ions in the plasma may be weakly or strongly coupled. Hence, it is useful for is an important but restricted subset of the problems we are interested in. Wave packet molecular dynamics (WPMD) offers the
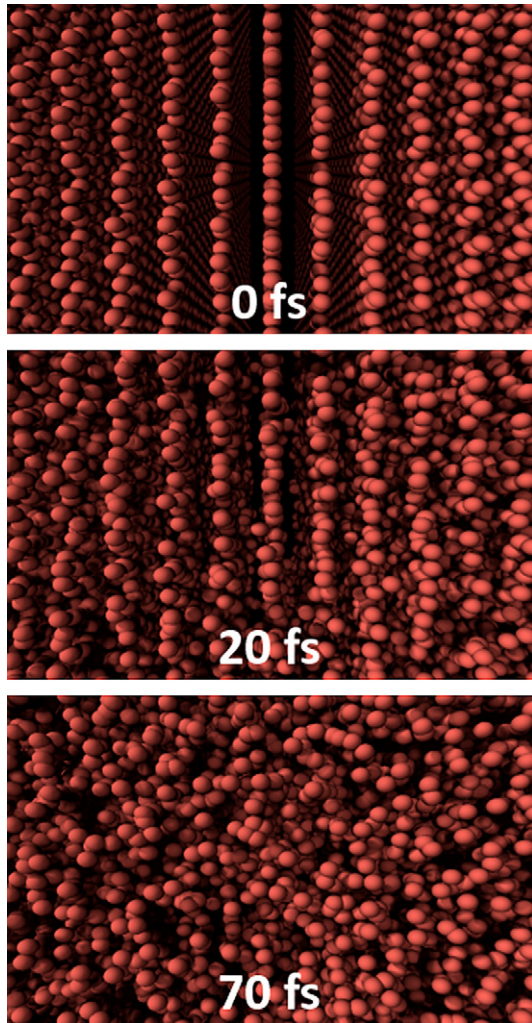
Fig. 17. Molecular dynamics simulation of the lattice structure of graphite exposed to an LCLS pulse.

distinct advantage of naturally incorporating quantum effects through the equations of motion. However, the extension of these methods to include radiative and atomic effects is still an area of research. While helping to address the QSP problem, they do not

address the time step issue discussed above. Kinetic theory molecular dynamics (KTMD) is a recent development and is based on leveraging the strengths of kinetic theory and MD for hot dense matter. The idea is to use a kinetic theory for the electrons and to treat the ions with MD. This method treats the quantum diffraction and interference effects through a quantum Wigner treatment of the electrons. The time step issue is resolved by solving the quantum kinetic equations for the electrons using an implicit time-stepping algorithm that is commensurate with the ion time scale. We emphasize that all of these are currently active areas of research. These alternatives are summarized in Table 2, which shows the advantages and disadvantages of each method. The remainder of this section is devoted to a discussion of these alternatives.

7.2. Orbital-free density functional theory

When calculating phenomena that do not require an explicit treatment of the electron dynamics, the Born-Oppenheimer approximation may be invoked, and the electronic structure can be calculated adiabatically given an ion configuration at every time-step. This is often referred to as quantum molecular dynamics (QMD), as MD is used to evolve only the ions. In almost all cases, the electronic structure arises from the solution of the Kohn-Sham orbitals within the context of density functional theory (DFT). The QMD method is computationally very expensive in comparison to other MD models for several reasons, including the fact that it employs many more, complex-valued functions that must be sampled on a fine mesh in reciprocal space, over many Brillouin zones. Worse is the enforcement of orbital orthonormality. However, the key limitation for computing the properties of high energy density materials is that the number of orbitals needed becomes prohibitively large as the temperature increases. To date, most QMD calculations are performed at zero temperature, with some in the few electron−volt range. To our knowledge, the highest temperature ever simulated using QMD is $T = 250$ eV, but this was a very difficult calculation that involved only *four* atoms [83].

A promising alternative to the approaches mentioned above is to return to the seminal theorems of DFT. In the original formulation of DFT, the basic variable is the density $n_e(r)$, which is a single real variable. Brillouin-zone sampling is not necessary since the density is computed in real space. The essential feature of what Hohenberg and Kohn proved was that this variable is, in principle, the only variable that is needed [84], however the proof is only one of existence and does not reveal the explicit forms. In particular, the

Table 2
Four methods of treating electron dynamics within an ion MD code are compared.

Method	Strongly-coupled ions	Strongly-coupled electrons	True electron dynamics	Fermi distribution function	Atomic physics	Pauli blocking
Statistical potentials	Yes	Yes. Accuracy depends on model chosen	No	No	Yes, in static limit. Main limitation is pair approximation, and independence of diffraction and Pauli	Somewhat. Static Pauli potentials account for effective repulsion
OF-DFT	Yes	Somewhat, depending on functional chosen	No	Yes	Somewhat, at extended Thomas-Fermi level	Electrons not dynamical
Wave-packet molecular dynamics	Yes	Yes	Yes	Somewhat, depending on particular choice of antisymmetry	Yes, but severely limited by Gaussian *ansatz* and approximate treatment of exchange	Yes, but limited by particular choice of antisymmetry (e.g., pair vs. full determinant)
Kinetic-theory molecular dynamics	Yes	Somewhat. Moderate coupling achieved through non-linear numerical solution. Extensions possible	Yes	Yes	Yes. Limited by kinetic model used, but contains atomic physics at least at the Thomas-Fermi level	Yes. Pauli blocking does not occur at mean-field level (WP system), but can be included in collision terms

kinetic energy proved to be quite difficult to find as a functional of the density; it was this problem that led to the re-introduction of orbitals, and the Kohn–Sham approach. Here, we return to the original, orbital-free DFT (OF-DFT) approach for three reasons. First, there has been substantial progress in finding kinetic energy functionals. Second, employing the density leads to much faster computational algorithms, which in turn makes it possible to simulate larger systems for longer periods of time. Third, for warm to hot dense matter, most of the subtle details of electronic structure are reduced due to thermal effects, and less precise functionals are needed.

Generally speaking, the equations to be solved are given by

$$\frac{1}{4\pi}\nabla^2\varphi = n_e(\mathbf{r}) - \sum_i Z_i\delta(\mathbf{r} - \mathbf{R}_i), \tag{43}$$

$$\ddot{\mathbf{R}}_i = -Z_i\nabla\varphi, \quad \frac{\delta\Omega}{\delta n_e} = 0, \tag{44}$$

where we have denoted the position of the ith ion as $\mathbf{R}_i$ with nuclear charge Z_i and the electric potential as φ. The entirety of the modeling is contained in accurately expressing the grand canonical potential $\Omega[n_e]$. The principal objective of this task will then be to develop a form of this potential which describes all the key physical processes while still maintaining a minimal computational complexity.

Shortly after Hohenberg and Kohn developed DFT for zero-temperature systems [84], Mermin extended the basic theorems to finite temperature [85]. In particular, these results show that the correct electron density is obtained by minimizing the grand canonical potential,

$$\Omega[n_e] = F_e[n_e] + \frac{1}{2}\iint d\mathbf{r}\,d\mathbf{r}'\frac{n_e(\mathbf{r})n_e(\mathbf{r}')}{|\mathbf{r} - \mathbf{r}'|} \tag{45}$$

$$+ \int d\mathbf{r}[v_{\text{ext}}(\mathbf{r}) - \mu]n_e(\mathbf{r}) + F_{\text{xc}}[n_e], \tag{46}$$

When this expression is minimized ($\delta\Omega[n_e]/\delta n_e(\mathbf{r})$=0), the resulting Euler–Lagrange equation yields the correct electronic density. In this expression, the first term on the right is the free energy of a non-interacting electron gas, and this term is the most difficult to determine in OF-DFT approaches. The next term describes the classical portion of the electron–electron interaction. The third term includes the interaction of the electrons with the nuclei in the molecular dynamics simulation as well as the chemical potential μ and is used to ensure the correct average density in the variational approach. The fourth and final term is the exchange-correlation contribution, which includes all quantum corrections missing from the other terms.

Suppose we neglect the exchange-correlation contribution, $F_{\text{xc}}[n_e]$, and use a form for $F_e[n_e]$ from a uniform electron gas; such an approximation is expected to be accurate for highly compressed matter. The uniform gas free energy is

$$F_e \approx F_{\text{TF}}[n_e] = \frac{\sqrt{2}}{\pi^2\beta^{5/2}}\int d\mathbf{r}\left[\eta\mathcal{I}_{1/2}(\eta) - \frac{2}{3}\mathcal{I}_{3/2}(\eta)\right] \tag{47}$$

with $n_e(\mathbf{r}) = \frac{\sqrt{2}}{\pi^2\beta^{3/2}}\mathcal{I}_{1/2}(\eta), \tag{48}$

where as before $\beta = 1/T$ is the inverse temperature, $\eta = \beta\mu$ is the degeneracy parameter, and $\mathcal{I}_p(\eta)$ is the usual Fermi integral of order p defined by

$$\mathcal{I}_p(\eta) \equiv \int_0^\infty \frac{x^p\,dx}{1 + e^{x-\eta}}. \tag{49}$$

Note that, as long as the electron density is nearly uniform, this scheme applies to materials of *any* nuclear composition (e.g., mixtures) at *any* temperature. In fact, this is nothing more than the Thomas–Fermi model cast in terms of the language of DFT, which has been applied to hot dense systems since the seminal work of Feynman, Metropolis, and Teller at Los Alamos during the Manhattan Project [86]. Their method can be applied here such that the resulting electron density is connected with many, potentially different ions that are evolved using molecular dynamics. Such a method has been used to simulate dense matter from $T = 0.1$ eV to $T = 5000$ eV [87]. It is important to note that this method is an all-electron, finite temperature method.

The Thomas–Fermi approximation, while enjoying many successes, has several well-known shortcomings such as predicting singularities in the density at ion centers, which is not only unphysical but also leads to numerical instabilities [87,88]. We propose to improve upon Eq. (47) by allowing for slowly-varying inhomogeneities. This can be done by including a finite-temperature gradient correction which yields the proper linear response in the long-wavelength limit [89]

$$F_e \approx F_{\text{TF}}[n_e] + F_{\text{GC}}\left[n_e, |\nabla n_e|^2\right] \tag{50}$$

where $F_{\text{GC}} = -\frac{1}{24}\int d\mathbf{r}\frac{d}{d\eta}\left(\frac{d\eta}{dn_e}\right)|\nabla n_e|^2. \tag{51}$

This correction changes the resulting Euler–Lagrange equation, which minimizes the functional, from an explicit expression of the electron density to a non-linear partial differential equation. While this adds some computational complexity, it resolves the singular densities and thus improves numerical stability. A further correction could be made to yield the *exact* linear response to all orders. One way to do this is to calculate the polarization function of the existing model, subtract this inherently inaccurate contribution off and then add on the exact linear response through the correct polarization function [90]

$$F_e \approx F_{\text{TF}} + F_{\text{GC}} + F_{\text{LR}}, \tag{52}$$

where $F_{\text{LR}} = \iint d\mathbf{r}\,d\mathbf{r}'n_e(\mathbf{r})\chi_{\text{model}}^{-1}(\mathbf{r} - \mathbf{r}')$

$$- \iint d\mathbf{r}\,d\mathbf{r}'n_e(\mathbf{r})\chi_{\text{LR}}^{-1}(\mathbf{r} - \mathbf{r}') \tag{53}$$

This again complicates the Euler–Lagrange equations, although computationally it only involves additional convolutions already being calculated. In Fig. 18, results from Ref. [90] are presented showing that systematic improvements to the kinetic energy functional yield more accurate results when compared to full DFT calculations. Here, all approximations are made at zero-temperature, where K_{DFT} is the DFT data, K_{LR} represents a functional *only* containing linear response, K_{TFW} is Thomas–Fermi (TF) with the so-called Weizsäcker correction, which is functionally similar to F_{GC}, and finally K_{TFLR} is TF corrected for exact linear response and gradient corrections as in Eq. (52). Note that as r_s goes to zero, i.e., the limit of high densities, K_{TFLR} produces the most accurate results.

7.3. Wave Packet Molecular Dynamics

In general, the time-dependent Schrödinger equation (TDSE) is very difficult to solve for a many-body system. However, we can
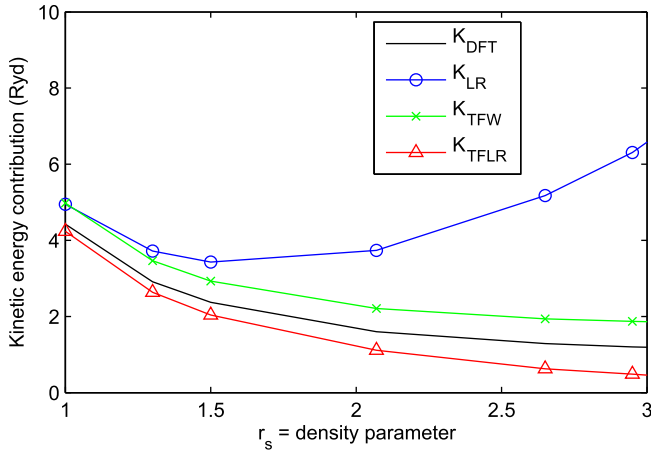
Fig. 18. Comparison of kinetic energy functional approximations with self-consistent DFT data for H in jellium [90]. K_{DFT} — DFT, K_{LR} — pure linear response, K_{TFW} — Thomas-Fermi (TF) with Weizsäcker term and K_{TFLR} — TF corrected for exact linear response. The density parameter $r_s = a_i/a_0$.

reduce the computational complexity via the use of a time-dependent variational principle (TDVP) [91–93]. To use this method, one must first define an action to vary. There are several possible choices [94]. Here, we discuss the stationary action principle

$$\delta \int dt \left\langle \psi \left| i\hbar \frac{\partial}{\partial t} - \hat{H} \right| \psi \right\rangle = 0. \quad (54)$$

The wave function is then written in terms of a finite number of time-dependent variational parameters.

$$|\psi\rangle = |\mathbf{Z}(\mathbf{t})\rangle = |z_1(t), z_2(t), \dots, z_n(t)\rangle. \quad (55)$$

One then varies with respect to $\mathbf{Z}^*$ to derive the equations of motion. Such equations of motion may require matrix inversion to solve, lead to too many equations, and/or have non-analytic terms. This motivates one to seek simple forms for $|\psi\rangle$ that are still able to model the requisite physics.

Heller [95] was the first to recognize that restricting the dynamics of a wave function to the Hilbert space consisting of Gaussian wave packets is a powerful semiclassical approximation. It is powerful in the sense that it leads to easy to evolve wave functions and easy to interpret results. The semiclassical approximation here is different than the usual $\hbar$ expansion. Instead, the classical approximation is identified with particles having exact positions and momenta, so this semiclassical approximation is that particles have approximate positions and momenta (the centers of the Gaussian wave function in its position and momentum representations, respectively) but do not violate the Heisenberg uncertainty principle. For quadratic potentials, this approximation is exact. Errors become large when the width of the packets is large or when third and higher derivatives of the potential become significant.

Wave Packet Molecular Dynamics (WPMD) is a simple way to implement quantum mechanics in a molecular dynamics code. WPMD extends the point particle dynamics to a dynamics of the Gaussian wave packet position, momentum, and width. It incorporates uncertainty in position and momentum consistent with the Heisenberg uncertainty principle and few-body exchange effects can be added while interference effects are still poorly treated.

The first application of WPMD to plasma physics was by Klakow, Toepffer, and Reinhard [96,97] and reviews are given by Littlejohn [98] and by Feldmeier and Schnack [91]. Such simulations were and

are important because they offer a dynamic replacement of quantum statistical potentials as well as a model that can be used to interpret molecular dynamics in a fully quantum mechanical way.

The equations of motion within the Gaussian restricted wave packet formalism of WPMD yield:

$$\dot{\mathbf{R}}_I = \frac{\mathbf{P}_I}{m_I}, \dot{\mathbf{r}}_i = \frac{\mathbf{p}_i}{m_e}, \dot{\gamma}_i = \frac{\eta_i}{m_e}, \quad (56)$$

$$\dot{\mathbf{P}}_I = \sum_{J \neq I} \frac{q_I q_J \mathbf{r}_{IJ}}{r_{IJ}^3} + \sum_{j \neq I} \frac{q_I q_j \mathbf{r}_{Ij}}{r_{Ij}^3} \left[\text{erf}\left(\sqrt{\frac{3}{2}} \frac{r_{Ij}}{\gamma_j} \right) - \frac{r_{Ij}}{\gamma_j} \sqrt{\frac{6}{\pi}} e^{-3r_{Ij}^2/2\gamma_j^2} \right] \quad (57)$$

$$\dot{\mathbf{p}}_i = \sum_J \frac{q_i q_J \mathbf{r}_{iJ}}{r_{iJ}^3} \left[\text{erf}\left(\sqrt{\frac{3}{2}} \frac{r_{ij}}{\gamma_j} \right) - \frac{r_{ij}}{\gamma_i} \sqrt{\frac{6}{\pi}} e^{-3r_{ij}^2/2\gamma_j^2} \right]$$
$$+ \sum_{j \neq I} \frac{q_i q_j \mathbf{r}_{ij}}{r_{ij}^3} \left[\text{erf}\left(\sqrt{\frac{3}{2}} \frac{r_{Ij}}{\gamma_{ij}} \right) - \frac{r_{Ij}}{\gamma_{ij}} \sqrt{\frac{6}{\pi}} e^{-3r_{ij}^2/2\gamma_{ij}^2} \right] \quad (58)$$

$$\dot{\eta}_i = \frac{9\hbar^2}{4m_e \gamma_i^3} + \frac{q_i}{\gamma_i^2} \sqrt{\frac{6}{\pi}} \left[\sum_J q_J e^{-3r_{ij}^2/2\gamma_i^2} + \sum_{j \neq I} \frac{q_j \gamma_i^3}{\gamma_{ij}^3} e^{-3r_{ij}^2/2\gamma_{ij}^2} \right], \quad (59)$$

where $\mathbf{r}_{ij} = \mathbf{r}_i - \mathbf{r}_j$, $\mathbf{r}_{iJ} = \mathbf{r}_i - \mathbf{R}_J$, $\mathbf{r}_{IJ} = \mathbf{R}_I - \mathbf{R}_J$, $\mathbf{r}_{Ij} = \mathbf{R}_I - \mathbf{r}_j$, $\gamma_{ij} = \sqrt{(\gamma_i^2 + \gamma_j^2)}$, m_I is the mass of ion I, and m_e is the electron mass. The indices i,j range over all the electrons and I,J range over all the ions. The trajectories from these equations of motion are softened in a similar fashion to a statistical potential. One difference is that the softening parameter (γ_i) is itself dynamic instead of the static thermal de Broglie wavelength used in statistical potentials. However, this comparison is not exactly a fair one. The positions and momenta mean different things (expectation values versus values in an ensemble used to sample the quantum partition function) and the softening arises due to these different interpretations.

The right hand side of Eq. (59) has two different terms which may give opposite behaviors. The first term represents a repulsion from having zero width. If the position is known very well, the momentum must be, by the Heisenberg uncertainty principle, very uncertain. So the particle can head off in any direction, e.g. spread. This is the only term that exists for a free particle and so it must eventually spread. Depending on temperature and density, the second term may or may not be strong enough to keep the widths from diverging.

7.4. Kinetic theory molecular dynamics

As discussed earlier, a limiting aspect of MD as applied to electron−proton plasmas is the restriction of the time step to electron collision time scales. For plasmas in the HDR regime, this means fractions of a fs. Ion electron collisions happen on a much longer time scale (factor of m_p/m_e) and thermonuclear burn on an even longer time scale of nanoseconds. Therefore, trying to run simulations of dense burning plasmas becomes impractical. It was recognized early on in the development of MD that the large discrepancy between the electron and ion time scales could be used to the computational physicist's advantage. In both Born−Oppenheimer MD [99] and Car−Parrinello MD [99,100], it is assumed that the electrons adapt rapidly to the changes in the ion positions and momenta. In the case of Born−Oppenheimer MD, the electron configuration is always assumed to be in a ground state which is computed from a stationary Schrodinger equation. Electron "dynamics" is a result of the effect of the classical ion dynamics on the electrons. In other words, the ground state electron configuration is updated with every change in the ion positions and momenta. In Car−Parrinello MD, there is recognition of the

separation of fast (electron) and long (ion) time scales. This translates into an adiabatic separation of energy scales. The beauty of their approach is that the electron–ion plasma can be mapped onto an equivalent classical description consisting of dynamic ions and electron orbitals.

The philosophy behind KTMD is based on several observations about HDR plasmas. First, the electrons are non-degenerate and weakly coupled. Second, the ions can be weakly or strongly coupled. KTMD attempts to take advantage of these properties along with the observations that: (1) MD is very good at moving classical particles around and computes their correlations exactly (2) Kinetic theory is well developed for weakly coupled plasmas. Hence, the approach of KTMD is to describe the electron dynamics fully with a kinetic equation and leave the ion dynamics to MD. HDR plasmas exhibit quantum effects at short distances and classical screening behavior at long distances. Therefore, the starting point for a kinetic theory description of the electron dynamics will be the Wigner equation with exchange effects ignored [101–103].

The process for deriving the relevant KTMD equations is straightforward although the calculations themselves are lengthy. For this paper, a description of the derivation is given; a separate longer paper will provide more details. The approach is based on starting with a Quantum Liouville (Wigner) equation for $N_e + N_p$ particles in a plasma where N_e refers to the number of electrons and N_p refers to the number of protons. This equation is used to construct the reduced Wigner distribution function for N_p protons. A closure scheme is required and it is assumed that higher order correlation functions can be written as a symmetrized sum of one-particle Wigner functions and pair correlation functions. This quantum Liouville description of the ion dynamics is used as the basis for the MD simulation and it describes the pushing of classical particles with effective forces [104]. The electron kinetic equation is derived from a single particle density operator. In the limit of weak coupling, a closed set of equations for the one particle electron Wigner function and the electron–electron and electron–proton pair correlation functions can be derived. This was done by Guernsey [104–106].

The numerical aspects of solving the KTMD equations are non-trivial. The approach we are taking is to first start with the quantum Vlasov form coupled to the Poisson equation. In this system, the pair correlations vanish. There are a vast number of classical methods for discretizing the quantum Vlasov system, such as particle-in-cell (PIC) [2], particle–particle–particle-mesh (P3M) [3], and the Eulerian (gridded Vlasov) [107] methods. However, the primary concern in the choice of a specific method for tackling the KTMD equations is that the quantum interaction term contains length scales that are in general much shorter than those typically associated with the methods mentioned above. The ideal method will be one that combines the simplicity and computational efficiency of the classical methods with the efficiency and accuracy to handle multiple length and timescales. It is well known that the Vlasov–Poisson system is dissipative [108,109], meaning that the quantum initial distribution will relax toward a Maxwellian distribution in time. Therefore, we must invoke a collisional term to effectively drive the distribution function toward some quantum equilibrium distribution. The subtlety here is that this equilibrium is time-dependent; each self-consistent time step taken within the KTMD method will lead to different equilibrium distribution. A starting point for this is a simple Bhatnagar–Gross–Krook (BGK)-type [110] collision model.

8. Comparisons of different methods for single electron dynamics

It is impossible to solve the TDSE for millions of particles in a real plasma, but an accurate solution is possible for a few electrons and protons. Therefore it is useful to make a comparison between various methods of interest (including the workhorse QSP) and the exact quantum mechanical solution for few body collisions. Here we consider (binary) electron–proton scattering and a single electron scattering from many protons. Such comparisons can inspire improvements in the approximate methods, as well as help us to understand which quantum effects dominate the physical systems of interest. Besides QSPs, our comparisons involve: (1) machine-accuracy (called "exact") solutions generated by the SOFT method; (2) a method (WCD) that preserves the initial properties of the wavefunction, but does not include interference; and (3) a method (WPMD) that employs simple Gaussian wavefunctions. The first two of these are described below; WPMD was described in Section 7.3.

8.1. Exact TDSE: Split Operator Fourier Transform method (SOFT)

For single-electron problems, the Schrödinger equation is

$$i\hbar \frac{\partial}{\partial t} \psi(\mathbf{r}) = \left(\frac{\hat{\mathbf{p}}^2}{2m_e} + V(\mathbf{r}) \right) \psi(\mathbf{r}), \tag{60}$$

$$V(\mathbf{r}) = -\sum_m \frac{eq_m}{|\mathbf{r} - \mathbf{R}_m|}, \tag{61}$$

where the sum is over all fixed scattering centers of charge q_m, located at positions $\mathbf{R}_m$. Eq. (58) is solved by repeated application of the propagation operator for a time step Δt, approximated by the split operator [111–115]

$$U(t, t+\Delta t) \approx \exp\left[-V\frac{\Delta t}{2} \right] \exp\left[-\frac{\hat{\mathbf{p}}^2}{2m_e}\Delta t \right] \exp\left[-V\frac{\Delta t}{2} \right]. \tag{62}$$

(where again $\hbar = 1$ for convenience). The Split Operator Fourier Transform (SOFT) method takes advantage of this factorization by applying the first operator in position space, the second in momentum space, and the third in position space because these operators are, respectively, diagonal in these spaces. The basis change from coordinate space to momentum space and vice versa is effected by forward and backward Fast Fourier Transforms on an equidistant grid.

The complex wave function $\psi(t)$ at time t is represented on the grid

$$r_{\alpha k} = r_{\alpha 0} + k \cdot \Delta x, \ k = 1, \ldots, 128$$

where α enumerates the three Cartesian directions. Here $r_{10} = -4$ Å, $r_{20} = r_{30} = -5$ Å, and $\Delta x = 10/128$ Å, small enough to correctly represent the momenta of the wave function at the energy range given (1 keV and below). The time step chosen is $\Delta t = 10^{-4}$ fs to accurately resolve the electron dynamics.

8.2. Wigner classical dynamics (WCD)

In this approach to improving the description of particle dynamics, one replaces a single point particle by a distribution of point particles whose density in phase space reproduces the quantum density. A classical propagation of these particles can then illuminate whether the width of the wave function is the dominant quantum effect in the process studied.

Given a three-dimensional Gaussian wave function as an initial single particle state (in this subsection we set $\hbar = 1$),

$$\psi_0(\mathbf{r}) = \left(2\pi\sigma_r^2 \right)^{-3/4} \exp\left(-\frac{(\mathbf{r} - \mathbf{r}_0)^2}{4\sigma_{\mathbf{r}}^2} + i\mathbf{p}_0 \cdot (\mathbf{r} - \mathbf{r}_0) \right) \tag{63}$$

with initial position $\mathbf{r}_0$ and initial momentum $\mathbf{p}_0$, the initial phase-space density is given by the Wigner distribution [116]

$$P(\mathbf{r}, \mathbf{p}) = \frac{1}{(2\pi)^3} \int_{-\infty}^{\infty} \psi^*\left(\mathbf{r} + \frac{\mathbf{s}}{2}\right) \psi\left(\mathbf{r} - \frac{\mathbf{s}}{2}\right) e^{i\mathbf{p}\cdot\mathbf{s}} \, d\mathbf{s}$$

$$= \frac{1}{(2\pi\sigma_{\mathbf{r}}\sigma_{\mathbf{p}})^3} \exp\left[-\frac{(\mathbf{r} - \mathbf{r}_0)^2}{2\sigma_{\mathbf{r}}^2} - \frac{(\mathbf{p} - \mathbf{p}_0)^2}{2\sigma_{\mathbf{p}}^2} \right] \qquad (64)$$

where the uncertainty relation gives $\sigma_{\mathbf{r}}\sigma_{\mathbf{p}} = 1/2$.

This six-dimensional Gaussian distribution in coordinate and momentum space was used for the Monte-Carlo initialization of a distribution of point particles whose particle density reproduces the quantum-mechanical density [117]. To perform Wigner Classical Dynamics [118], these particles were propagated due to Newton's equations of motion using the Velocity–Verlet method [119]. A complication arises when an electronic particle experiences a close encounter with a proton − the gradient of the Coulomb potential then becomes divergent. To solve this problem, the analytic solution of the Kepler problem for this two-body problem is applied to position and momentum, which are then updated according to the gradients of the Coulomb potential due to the remaining protons.

Using an adaptive time step to converge the energy drift, this mixed method performs faster than standard integrators. It is different from existing variable regularization schemes popular in astrophysics [120−125] in that it does not require keeping track of variable and time transformations or alignment of time steps between the regularized and the remaining part of the system. It can thus be treated as a black box method that can be added to existing dynamics codes easily. The algorithm used for the solution of the Kepler problem and its implementation are based on a vectorial solution [126]. The mixed analytic solution with numerical update method is described and its performance analyzed in detail in a separate publication [127]. The test particles in the WCD method do not interact, a feature that offers obvious parallelizability.

8.3. Binary scattering

We first consider an electron scattered by its interaction with a (fixed) proton, and compare in detail various classical and quantum trajectory results. In the classical view, the electron samples the interaction only at points on the trajectory, while in the quantum view, it continually samples the Coulomb interaction over an extended region (the wave packet).

We show in Fig. 19 electron trajectories given by the Dunn–-Broyles QSP for three different plasma temperatures. These are compared, in each case, with classical trajectories for a pure Coulomb potential and with various quantum expectation values of the electron position. In all cases, the initial total electron energy is 9.2 eV, and for SOFT, WCM and WPMD the initial condition is given by Eq. (63), with width $\sigma_{\mathbf{r}} = 0.05$ Å, position $x = -1$ Bohr, and impact parameter y in increasing multiples of 0.2 Bohr.

It can be seen that, as the QSPs are constructed to attempt to emulate quantum dynamics, all QSP trajectories curve less sharply around the proton (indicated by the black cross) than do their classical, pure Coulomb counterparts. However, the QSP trajectories curve more sharply than the quantum mechanical trajectories. Fig. 19 shows that the agreement of the QSP trajectory with the exact result (SOFT) is best at the lowest temperature, 4.6 eV. Even for this temperature the agreement is fairly good only at the largest impact parameter and the final time, and not as good at intermediate time. The QSP trajectory with the medium impact parameter agrees well with SOFT in the scattering region but not at long times.
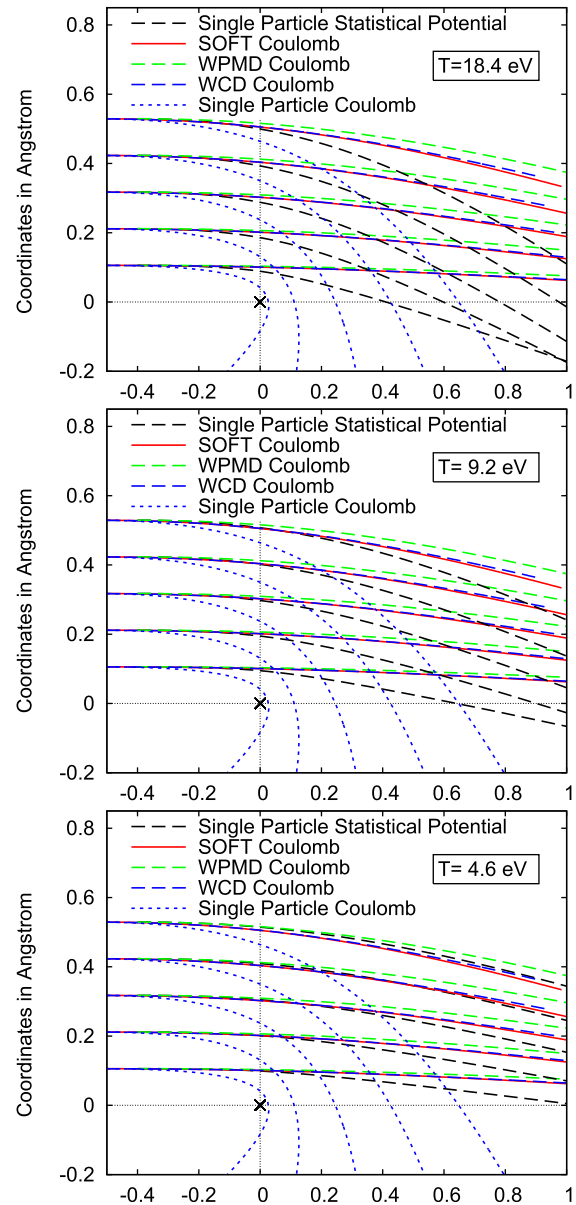
Fig. 19. Comparison of trajectories for a single electron scattering from a single proton. Shown are expectation values of the position evaluated using exact quantum mechanical SOFT (solid red), approximate quantum mechanical WPMD (dashed green), and quantum-classical WCD (dashed blue) methods, versus positions of classical single particles in the Coulomb (dotted blue) and Dunn-Broyles statistical potentials (dashed black). The electron energy is 9.2 eV and the results shown correspond to QSP at plasma temperatures 18.4 eV, 9.2 eV, and 4.6 eV. It can be seen that agreement of QSP trajectories with those of quantum methods depends on the temperature as well as the impact parameter. (For interpretation of the references to colour in this figure legend, the reader is referred to the web version of this article.)

This demonstrates that it is not possible to match qualitative quantum behavior with the QSP point particles, as agreement of the trajectories depends on the temperature as well as the impact parameter. In the QSP model the particles have no width but the interaction potential is softened. The other methods, by contrast, feature finite-radius particles that interact with the Coulomb potential. Fig. 19 shows that these methods give trajectories that agree well with the exact result despite having no adjustable temperature parameter.

Overall, we note that for what should be the same interaction (same initial conditions), different results are obtained with QSPs.

This is due to the problematic assumption that a temperature can be associated with a single electron. In an MD simulation, different energy electrons interact with nuclei through the same potential corresponding to an average temperature. However, electrons of the same energy that are propagated in MD simulations of different temperature interact with the nuclei through different potentials, which leads to different outcomes of the scattering events.

The exact quantum trajectory follows a softened trajectory with respect to the single particle classical result. This is due to the electron sampling the potential over the range of its width, and is qualitatively similar to the QSP result. However, the reason for the softening of the trajectory in the statistical potential is distinct from that in the quantum mechanical case. The positions and momenta in QSP dynamics are not real positions and momenta. These virtual dynamics are constructed solely to get the right statistics in thermal equilibrium. Therefore, *individual* trajectories should not be used to make any statements about observables, such as radiation produced by the acceleration of electrons.

We now compare SOFT, WPMD, and WCD. For these comparatively low energies, WCD yields trajectories following those from the exact SOFT method more closely than the ones from WPMD. This is because the electrons in the current WPMD approach are represented by isotropic Gaussian wave packets. Hence they can neither deform into anisotropic densities, nor bifurcate into bound and unbound components. Both of these degrees of freedom are open for the multiple particles representing the electron density in the WCD approach, allowing for the observed improvement of the trajectories. This is in spite of WCD using only classical equations of motion, indicating a dominance of width effects (sampling of different portions of the potential) when switching from classical to quantum dynamics.

8.4. Quantum pinball

To gain a better understanding of the dominant quantum effects in electron dynamics in a plasma, scattering of a single electron from a disordered array of protons was simulated using SOFT, WPMD, and WCD. This test is different from electron–proton scattering in that interference may occur between components of the wave function scattered off different scattering centers. Quantum cross sections are therefore not additive, potentially resulting in deviations from a classical prediction.

A cluster of 125 protons, spanning $5 \times 5 \times 5 \text{ Å}^3$, corresponding to a plasma density of

$$\rho_{\text{plasma}} = 1\text{Å}^{-3} = 10^{24} cm^{-3}$$

was placed centrally at the coordinate origin. Electronic wave packets were placed at the boundary and launched with a range of initial momenta typical of plasma energies. Resulting electron densities were compared to ascertain the accuracy of the methods employed.

Our test is to give each method the same initial wave function, shown in Fig. 20 and given in Eq. (63), where $\mathbf{r}_0 = (-2.4 \text{ Å},0,0)$ is the initial expectation value of the position, $\sigma_r = 0.3458\text{Å}$ the initial width, and $\mathbf{p}_0 = (p_0,0,0)$ the initial expectation value of momentum. The initial width σ was chosen from a Gaussian fit to the 1s state of the hydrogen atom, so that the initial wave packet can be thought of as a free electron resulting from the recent ionization of a hydrogen atom. The initial momenta were chosen so that $p_0^2/2m_e$ is 1 keV, 250 eV, and 62.5 eV, respectively, for the three cases compared here. The accuracy of WPMD and WCD can be quantified by comparing the densities evolved with the different models at some later time.

Fig. 21 shows as small gray dots the point particles propagated with the WCD method and as blue outlines the number density
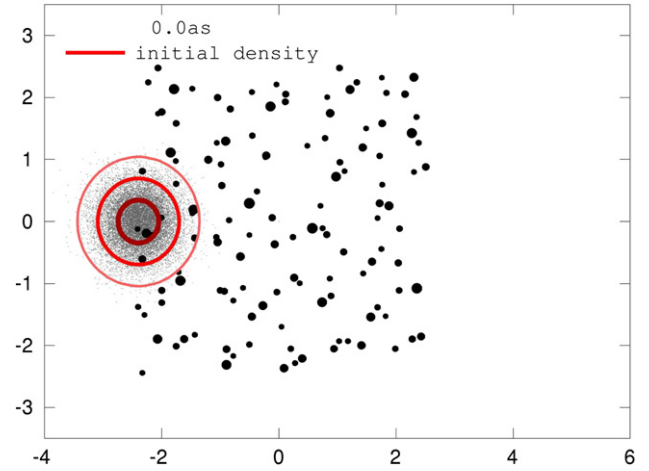

Fig. 20. Contour plots of initial density, integrated over the z coordinate. Coordinate axes are in Angstroms. Contours are drawn at percentages of the maximum density found at $1 \times \sigma$, $2 \times \sigma$ and $3 \times \sigma$ from the center of a Gaussian. Small black dots represent initial positions of particles for the Wigner Classical Dynamics (WCD) method. Proton coordinates are shown as black dots, larger for protons closer to the $z = 0$ plane in which the initial wave function is centered.

collected in 64^2 quadratic bins covering the quantum grid. (Each bin covers 2^3 quantum grid cells.) For illustration purposes, particles shown are from a simulation using $5^6 = 15,625$ particles. Contour lines and quantitative measures shown in Table 3 are derived from simulations using $7^6 = 117,649$ particles. A maximum allowed energy drift of $2.72 \cdot 10^{-2}$ eV/fs for each particle was used as the basis for the adaptive time step simulations with a smallest allowed time step of 10^{-39} s (!).

Fig. 21 also shows contour maps of SOFT probability densities $\rho(\mathbf{r}) = \psi^*(\mathbf{r})\psi(\mathbf{r})$ (red outlines) after passing through the proton cluster for the three initial kinetic energies. Contours are drawn at percentages of the maximum density found at the single, double, and triple width of a Gaussian distribution. Snapshots were taken at different times owing to the varying velocities with which the wave packet progresses, such that the electron density has just left the proton cluster at that time.

Because the energies are so high, scattering is generally weak in the examples considered. For that reason, it is relatively easy for a model to reproduce the exact dynamics. In order to understand exactly what part of the dynamics is nontrivial, we have also included the evolution of a free wave packet (zero potential). This is shown as the gray contours in Fig. 21. A comparison with the analytic density shows that the protons act on the wave packet through acceleration, deformation, and suppression of dispersion.

Fig. 21 shows final densities resulting from WPMD simulation as green contours.

Agreement between the final densities shown in Fig. 21 for methods A and B can be evaluated using the normalized overlap term

$$\Omega_{A-B}^{T_0} = \frac{\displaystyle\int_V \varrho_A^{1/2} \varrho_B^{1/2} d\mathbf{r}}{\left(\displaystyle\int_V \varrho_A d\mathbf{r}\right)^{1/2} \cdot \left(\displaystyle\int_V \varrho_B d\mathbf{r}\right)^{1/2}}, \quad (65)$$

where T_0 is the initial kinetic energy and ϱ_X is the final density for method X. For perfect agreement between the densities predicted by methods A and B,
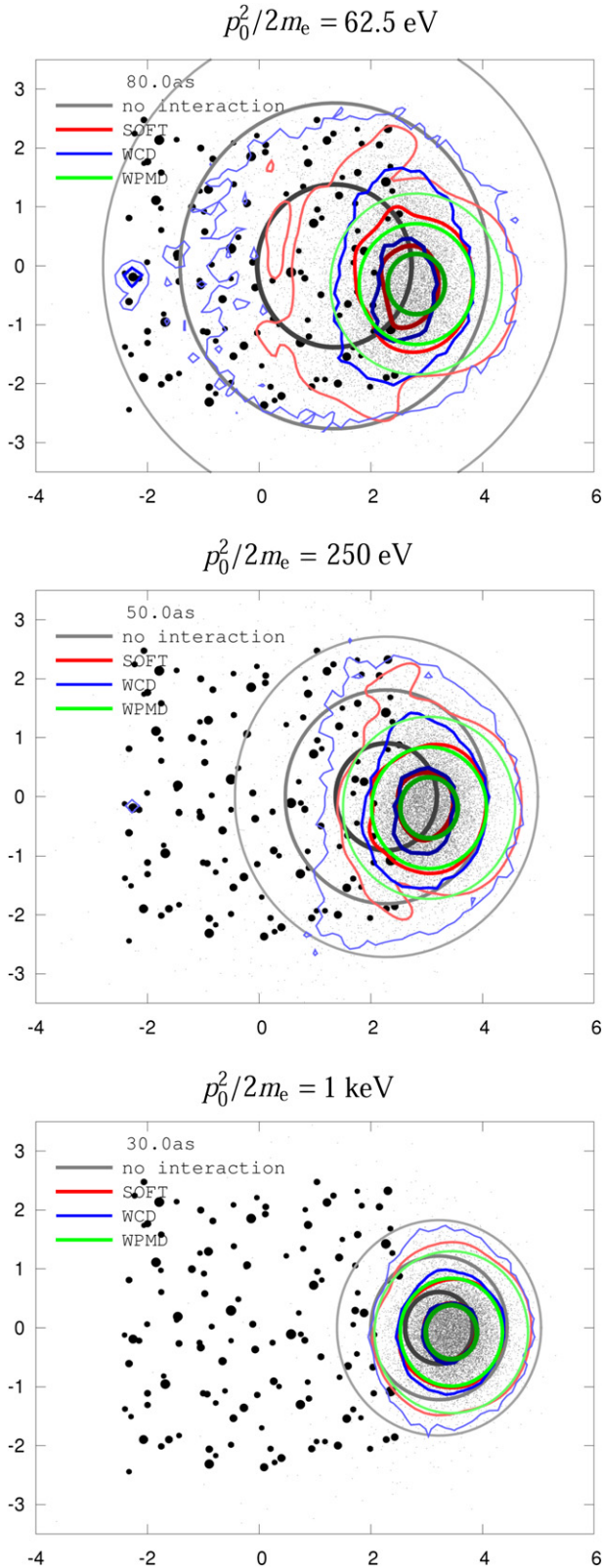
Fig. 21. Contour plots of the probability densities given by different methods after passing through the proton cluster, integrated over the z coordinate. Coordinates in Å. SOFT (red contour lines), WPMD (green contour lines), WCD (small particles and blue contour lines), and no interaction (dark contour lines). Protons (black dots), shown as larger for protons closer to the $z = 0$ plane. (For interpretation of the references to colour in this figure legend, the reader is referred to the web version of this article.)

Table 3
Agreement of final densities shown in Fig. 21 quantified by the normalized overlap $\Omega_{A-B}^{T_0}$, eq. (62) for three different initial kinetic energies and three methods discussed in this section.

T_0 [eV]	Method A	Method B	$\Omega_{A-B}^{T_0}$
1000	SOFT	WPMD	0.90
1000	SOFT	WCD	0.97 ± 0.01
1000	WPMD	WCD	0.90 ± 0.01
250	SOFT	WPMD	0.97
250	SOFT	WCD	0.91 ± 0.01
250	WPMD	WCD	0.90 ± 0.01
62.5	SOFT	WPMD	0.89
62.5	SOFT	WCD	0.86 ± 0.01
62.5	WPMD	WCD	0.75 ± 0.01

$$\Omega_{A-B}^{T_0} = 1. \qquad (66)$$

Densities were used as the basis of our comparison throughout, as the wave function's phase is unavailable in the WCD method.

Table 3 shows normalized overlap values $\Omega_{SOFT-WPMD}^{T_0}$ for the three initial kinetic energies used. All are at or above 0.9, which means that WPMD not only reproduces the SOFT trajectory, but also the wave packet's time-dependent dispersion for the scattering problem at multiple Coulomb potentials. Even in the lowest kinetic energy case, which results in a more strongly deformed final SOFT quantum density, the isotropic WPMD packet covers the main features of the SOFT density, confirming the WPMD method's viability for electron scattering at a proton cluster.

As can be seen in Table 3, agreement of the final density between SOFT and WCD systematically declines with lowered initial kinetic energy. This is due to

1. The increased total time of the simulation until the density leaves the proton cluster allowing the simulation to accrue deviation and
2. A systematic overestimation by the WCD method as to what fraction of the wave function is bound compared to SOFT, as can be seen in the blue contour lines on the left hand's side present in Fig. 21.

The Wigner particle density method can be systematically improved by

1. extending the equations of motion for the particles to sample forces at certain distances away from their position [128] or
2. associating a phase with each particle that correctly accounts for quantum superposition in the binning process underlying the contour levels.

However, classical dynamics of the Wigner particle density already yields good agreement with the SOFT result, so that it can be concluded that the dominant quantum effect for an electron scattering off a proton cluster is due to the width of the wave packet rather than interference effects.

Since one of the controversial issues about WPMD is the spreading of the widths, it is useful to compare the evolution of the width against SOFT. We also include WCD to show how much of the spreading is due to the uncertainty in position and momentum. These comparisons are shown in Fig. 22. Due to the difference in one-dimensional and three-dimensional widths, $\sigma = \gamma/\sqrt{3}$. For all three thermal velocities of the initial wave packet shown (1 keV, 250 eV, and 62.5 eV), WPMD actually *underestimates* the width while WCD overestimates it. Interference between the scattered waves is important for confining the wave packet and this effect is overestimated by WPMD owing to its restriction to an isotropic
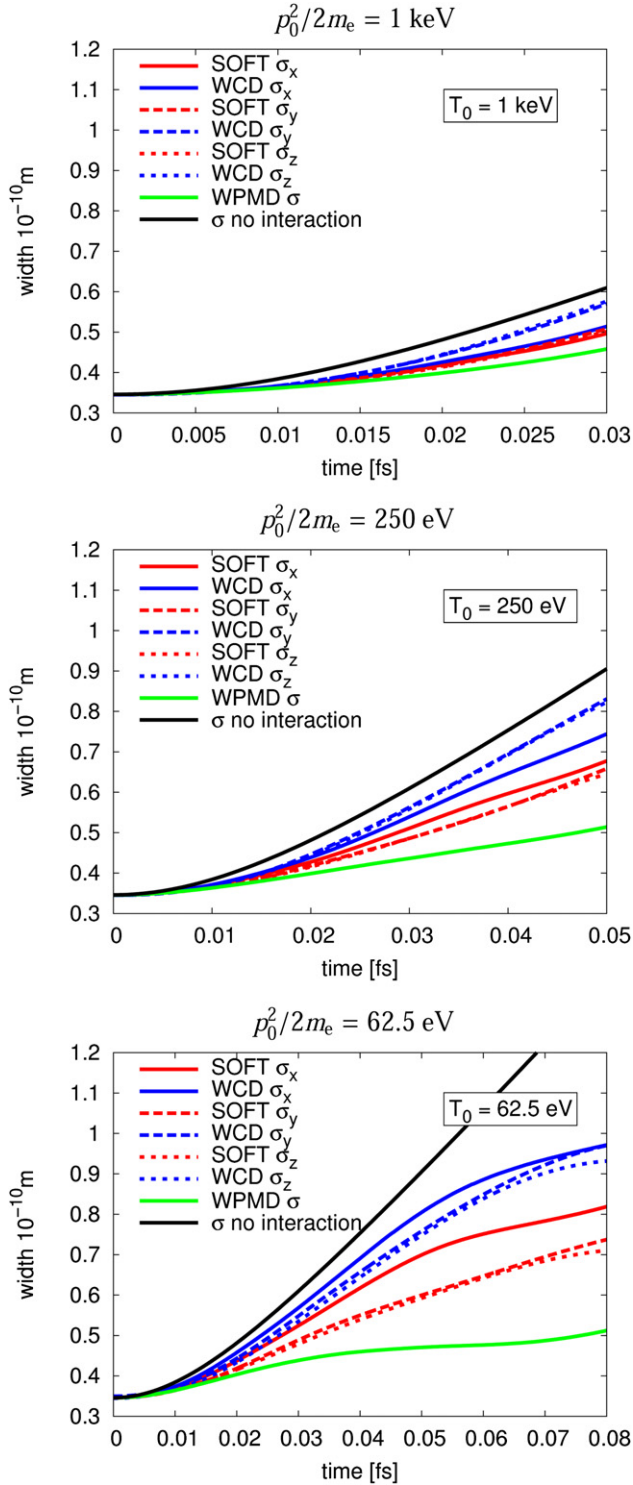
Fig. 22. Width evolution given by different methods after passing through the proton cluster: SOFT (red lines), WPMD (green lines), WCD (blue lines), and no interaction (black lines). (For interpretation of the references to colour in this figure legend, the reader is referred to the web version of this article.)

tails of the SOFT density have, however, a large weight in the calculation of the width σ. Also shown in the plots is the evolution of the free wave packet. The width in this evolution is always greater than that for the non-zero potential, showing that the nuclei help to confine the packet. We emphasize that these are very short evolutions (tens of attoseconds), and so we cannot draw any conclusion about the large-time fate of the widths (whether they diverge or eventually decrease).

The widths for each of the Cartesian directions are shown in Fig. 22 for anisotropic wave packets. Note that the black lines in all three graphs represent the same time-dependence of the free electron width and that the time scales of the graphs differ. SOFT generally predicts the packets to be less confined in the direction of motion (x coordinate) than in the y and z directions. WCD has a tendency to the opposite, except in the lowest energy case (62.5 eV). Fig. 21 reveals, however, that in this case a considerable fraction of the test particles are bound by the proton first encountered and remain there (in the exact quantum calculation, some density is left there too, but to a much smaller extent). Owing to their large distance from the final position, these bound particles contribute disproportionately to the x component of the width, hiding the tendency of the unbound part to have a smaller width in the x direction, which becomes apparent to the eye in Fig. 21. It must be concluded that interference effects, which make SOFT widths smaller in general than WCD widths, act more strongly in the y and z direction. Common to all graphs of Fig. 22 is that the width of the free packet is an upper bound, demonstrating that the net effect of the proton cluster is that of focusing the packet.

Several important properties of a real plasma are ignored in our quantum pinball test problems, and in the future we plan to address the following points:

1. The scattering centers are all positively charged. This may bias the wave packet toward being more confined compared to what exists in a neutral plasma.
2. A real plasma is usually macroscopic and so it is unlikely that an electron will encounter its boundaries. This can be modeled by introducing a periodic potential and periodic boundary conditions on the sides of our box of protons.
3. Degeneracy effects may also be important, especially at lower energies.

9. Cimarron prospectus

The MD simulation capability provides insight into the behavior of hot dense plasmas. We are now just beginning to mine the potential of this tool for investigating a wide range of physical processes in plasmas. We have presented new results for two of these, electron–ion coupling and charged particle stopping. Future work will be directed toward evaluating thermal conductivities, diffusivity and EOS. In addition, plasma mixtures are ripe for investigation by MD simulations. We will be investigating the properties of plasmas where a high-Z ion component is strongly coupled while the proton–proton component is weakly coupled. This will provide an interesting test of the assumptions underlying current theoretical treatments of plasma mixtures.

Another area of application for the MD simulation capability presented here is integrated, or multi-physics, problems. Unfortunately, this class of problems typically is beset by disparate time scales. Future directions will adapt the traditional MD concept by making use of the advantages of kinetic theory and molecular dynamics. Of particular interest is the ability to perform fundamental MD simulations of hot dense plasmas undergoing thermonuclear burn. Low- and high-Z mixtures again will provide an

shape, and underestimated owing to the absence of phase information in WCD. However, as shown by the overlaps given in Table 3, this effect does not dominate at short timescales. In fact, close inspection of Fig. 21 shows that WPMD reproduces the large density portions of the SOFT wave function very well, while ignoring deformations at the lowest-density contour level. The long

interesting test of the effects of screening on reaction rates and heating of the plasmas due to charged particle energy deposition.

Moving past the quantum statistical potentials will be a key area of research that will impact both the component and integral physics topics discussed above. KTMD may provide the first exact potentials useful for non-equilibrium plasmas. WPMD continues to offer interesting possibilities, especially in light of the fact that we can test the validity of its underlying assumptions through comparisons with exact, time-dependent quantum mechanics.

Acknowledgments

References

[1] S. Azteni, J. Meyer-ter-Vehn, The Physics of Inertial Fusion, second ed. Clarendon Press, Oxford, 2004.
[2] C.K. Birdsall, A.B. Langdon, Plasma Physics via Computer Simulation, Adam Hilger, New York, 1991.
[3] R.W. Hockney, J.W. Eastwood, Computer Simulation Using Particles, McGraw Hill Company, New York, 1981.
[4] K. Sanbonmatsu, L. Thode, H. Vu, M. Murillo, Comparison of molecular dynamics and particle-in-cell simulations for strongly coupled plasmas, Journal de Physique IV (Proceedings) 10 (2000) 259–262 EDP Sciences, Les Ulis.
[5] L. Spitzer Jr., Physics of Fully Ionized Gases, second ed. Interscience, New York, 1962.
[6] C.S. Jones, M.S. Murillo, Analysis of semi-classical potentials for molecular dynamics and monte carlo simulations of warm dense matter, High Energy Density Physics 3 (3–4) (2007) 379–394.
[7] B.J. Alder, T.E. Wainwright, Studies in molecular dynamics. i. general method, The Journal of Chemical Physics 31 (2) (1959) 459–466.
[8] W.C. Swope, H.C. Andersen, P.H. Berens, K.R. Wilson, A computer simulation method for the calculation of equilibrium constants for the formation of physical clusters of molecules: application to small water clusters, The Journal of Chemical Physics 76 (1) (1982) 637–649.
[9] P.J. Channell, C. Scovel, Symplectic integration of hamiltonian systems, Nonlinearity 3 (2) (1990) 231.
[10] M.P. Allen, D.J. Tildesley, Computer Simulation of Liquids, Clarendon Press, New York, NY, USA, 1989.
[11] H.C. Andersen, Molecular dynamics simulations at constant pressure and/or temperature, The Journal of Chemical Physics 72 (4) (1980) 2384–2393.
[12] H.J.C. Berendsen, J.P.M. Postma, W.F. van Gunsteren, A. DiNola, J.R. Haak, Molecular dynamics with coupling to an external bath, The Journal of Chemical Physics 81 (8) (1984) 3684–3690.
[13] W.G. Hoover, Canonical dynamics: equilibrium phase-space distributions, Physical Review A 31 (3) (1985) 1695–1697.
[14] A. Brünger, C.L. Brooks, M. Karplus, Stochastic boundary conditions for molecular dynamics simulations of st2 water, Chemical Physics Letters 105 (5) (1984) 495–500.
[15] J.E. Jones, On the determination of molecular fields. II. From the equation of state of a gas, Proceedings of the Royal Society of London. Series A 106 (738) (1924) 463–477.
[16] J.A. Moriarty, J.F. Belak, R.E. Rudd, P. Söderlind, F.H. Streitz, L.H. Yang, Quantum-based atomistic simulation of materials properties in transition metals, Journal of Physics: Condensed Matter 14 (11) (2002) 2825.
[17] D.W. Brenner, Empirical potential for hydrocarbons for use in simulating the chemical vapor deposition of diamond films, Physical Review B 42 (15) (1990) 9458–9471. doi:10.1103/PhysRevB.42.9458.http://dx.doi.org/10.1103/PhysRevB.42.9458.
[18] J. Tersoff, New empirical approach for the structure and energy of covalent systems, Physical Review B 37 (12) (1988) 6991–7000.
[19] M.W. Finnis, J.E. Sinclair, A simple empirical n-body potential for transition metals, Philosophical Magazine A 50 (1) (1984) 45–55.
[20] J. Hansen, I. McDonald, Microscopic simulation of a strongly coupled hydrogen plasma, Physical Review A (General Physics) 23 (1981) 2041–2059.

[21] J.-P. Hansen, I.R. McDonald, Theory of Simple Liquids, third ed. Academic Press, Amsterdam, 2006.
[22] J. Hansen, G. Torrie, P. Vieillefosse, Statistical mechanics of dense ionized matter. VII. Equation of state and phase separation of ionic mixtures in a uniform background, Physical Review A (General Physics) 16 (1977) 2153–2168.
[23] B. Bernu, J.-P. Hansen, Thermal-conductivity of a strongly coupled hydrogen plasma, Physical Review Letters 48 (1982) 1375–1378.
[24] J.-P. Hansen, I.R. McDonald, Thermal relaxation in a strongly coupled 2-temperature plasma, Physics Letters A 97 (1983) 42–44.
[25] C. Sagui, T. Darden, Molecular dynamics simulations of biomolecules, Annual Review of Biophysics & Biomolecular Structure 28 (1999) 155–179.
[26] C. Sagui, T. Darden, Multigrid methods for classical molecular dynamics simulations of biomolecules, Journal of Chemical Physics 114 (2001) 6578–6591.
[27] Y. Shan, J.L. Klepeis, M.P. Eastwood, R.O. Dror, D.E. Shaw, Gaussian split Ewald: a fast Ewald mesh method for molecular simulation, Journal of Chemical Physics 122 (5) (2005).
[28] E.L. Pollock, J. Glosli, Comments on P3M, FMM, and the Ewald method for large periodic coulombic systems, Computer Physics Communications 95 (1996) 93–110.
[29] D.F. Richards, J.N. Glosli, B. Chan, M.R. Dorr, E.W. Draeger, J.-L. Fattebert, W.D. Krauss, T. Spelce, F.H. Streitz, M.P. Surh, J.A. Gunnels, Beyond homogeneous decomposition: scaling long-range forces on massively parallel systems, in: Proceedings of the Conference on High Performance Computing Networking, Storage and Analysis, SC '09, ACM, New York, NY, USA, 2009, pp. 60:1–60:12.
[30] Lammps benchmarks, http://lammps.sandia.gov/bench.html.
[31] R.P. Feynman, Statistical Mechanics, Benjamin/Cummings Publishing Company, Inc., Reading, MA, 1972.
[32] D.M. Ceperley, Path integrals in the theory of condensed helium, Review of Modern Physics 67 (2) (1995) 279–355.
[33] H.F. Trotter, On the product of semi-groups of operators, Proceedings of the American Mathematical Society 10 (1959) 545–551.
[34] E.L. Pollock, Properties and computation of the coulomb pair density matrix, Computer Physics Communications 52 (1) (1988) 49–60.
[35] R. Storer, Path-integral calculation of the quantum-statistical density matrix for attractive Coulomb forces, Journal of Mathematical Physics 9 (1968) 964–970.
[36] A. Klemm, R. Storer, The structure of quantum fluids: helium and neon, Australian Journal of Physics 26 (1973) 43–59.
[37] G. Kelbg, Theorie des quanten-plasmas, Annalen der Physik 12 (1963) 219–224.
[38] A. Filinov, M. Bonitz, W. Ebeling, Improved Kelbg potential for correlated Coulomb systems IOP Publishing, UK, Journal of Physics A (Mathematical and General) 36 (2003) 5957–5962 International Conference on Strongly Coupled Coulomb Systems (SCCS), 2-6 September 2002, Santa Fe, NM, USA..
[39] G.E. Uhlenbeck, L. Gropper, The equation of state of a non-ideal Einstein-Bose or Fermi-Dirac gas, Physical Review 41 (1) (1932) 79–90.
[40] F. Lado, Effective potential description of the quantum ideal gases, Journal of Chemical Physics 47 (1967) 5369.
[41] C. Deutsch, M.M. Gombert, H. Minoo, Classical modelization of symmetry effects in the dense high-temperature electron gas, Physics Letters A 66 (1978) 381–382.
[42] C. Deutsch, M.M. Gombert, H. Minoo, Classical modelization of symmetry effects in the dense high-temperature electron gas: errata, Physics Letters A 72 (1979) 481–481.
[43] T. Dunn, A.A. Broyles, Method for determining the thermodynamic properties of the quantum electron gas, Physical Review 157 (1967) 156–166.
[44] M.W.C. Dharma-wardana, F. Perrot, Simple classical mapping of the spin-polarized quantum electron gas: distribution functions and local-field corrections, Physical Review Letters 84 (2000) 959–962.
[45] W.J. Mullin, G. Blaylock, Quantum statistics: is there an effective fermion repulsion or boson attraction? American Journal of Physics 71 (2003) 1223–1231.
[46] J. Glosli, F. Graziani, R. More, M. Murillo, F. Streitz, M. Surh, Molecular dynamic simulations with radiation, Journal of Physics A: Mathematical and Theoretical 42 (214030) (2009) 11.
[47] R. More, F. Graziani, J. Glosli, M. Surh, Radiation in particle simulations, High Energy Density Physics 6 (2010) 29–38.
[48] R. More, M. Goto, F. Graziani, P. Ni, H. Yoneda, Emission of visible light by hot dense metals, Plasma and Fusion Research 5 (2010) S2007.
[49] S. Byron, R. Stabler, P. Bortz, Electron-ion recombination by collisional and radiative processes, Physical Review Letters 8 (1962) 376–379.
[50] Y.-K. Kim, M. Rudd, Binary-encounter-dipole model for electron-impact ionization, Physical Review A (Atomic, Molecular, and Optical Physics) 50 (1994) 3954–3967.
[51] J. Yeh, I. Lindau, Atomic subshell photoionization cross sections and asymmetry parameters: 1 < or = /b Z/ < or = 103, Atomic Data and Nuclear Data Tables 32 (1985) 1–155.
[52] E. McGuire, K -shell Auger transition rates and fluorescence yields for elements Be-Ar, Physical Review 185 (1969) 1–6.
[53] H. Scott, Cretin-a radiative transfer capability for laboratory plasmas, Journal of Quantitative Spectroscopy and Radiative Transfer 71 (2001) 689–701.
[54] D.A. McQuarrie, Statistical Mechanics, second ed. University Science Books, Mill Valley, CA, 2000.

[55] J.P. Boon, S. Yip, Molecular Hydrodynamics, second ed. Dover Publications, Inc., New York, 1980.

[56] L.S. Brown, D.L. Preston, R.L. Singleton Jr., Charged particle motion in a highly ionized plasma, Physics Reports 410 (2005) 237.

[57] J. Daligault, G. Dimonte, Correlation effects on the temperature-relaxation rates in dense plasmas, Physical Review E 79 (2009) 056403.

[58] B. Jeon, et al., Energy relaxation rates in dense hydrogen plasmas, Physical Review E 78 (2008) 036403.

[59] J.N. Glosli, et al., Molecular dynamics simulations of temperature equilibration in dense hydrogen, Physical Review E 78 (2008) 025401(R).

[60] L.X. Benedict, et al., Molecular dynamics simulations of electron-ion temperature equilibration in an SF_6 plasma, Physical Review Letters 102 (2009) 205004.

[61] L.X. Benedict, et al., Molecular dynamics simulations and generalized Lenard-Balescu calculations of electron-ion temperature equilibration in plasmas, in preparation.

[62] D.O. Gericke, M.S. Murillo, M. Schlanges, Dense plasma temperature equilibration in the binary collision approximation, Physical Review E 65 (2005) 036418.

[63] D.O. Gericke, Kinetic approach to temperature relaxation in dense plasmas, Journal of Physics Conference Series 11 (2005) 111.

[64] J. Vorberger, D.O. Gericke, Th. Bornath, M. Schlanges, Energy relaxation in dense, strongly coupled two-temperature plasmas, Physical Review E 81 (2010) 046404.

[65] G. Zwicknagel, C. Toeppfer, P.-G. Reinhard, Stopping of heavy ions in plasmas at strong coupling, Physics Reports 309 (1999) 117–208.

[66] T. Peter, J.M. ter Vehn, Energy loss of heavy ions in dense plasma. i. linear and nonlinear vlasov theory for the stopping power, Physical Review A 43 (1991) 1998–2014.

[67] D.O. Gericke, M. Schlanges, Beam-plasma coupling effects on the stopping power of dense plasmas, Physical Review E 60 (1999) 904–910.

[68] J.F. Ziegler, J.P. Biersack, M.D. Ziegler, SRIM the Stopping and Range of Ions in Matter, SRIM Co., 2008.

[69] S.H. Glenzer, O.L. Landen, P. Neumayer, R.W. Lee, K. Widmann, S.W. Pollaine, R.J. Wallace, G. Gregori, A. Höll, T. Bornath, R. Thiele, V. Schwarz, W.-D. Kraeft, R. Redmer, Observations of plasmons in warm dense matter, Physical Review Letters 98 (2007) 065002.

[70] R. Thiele, T. Bornath, C. Fortmann, A. Höll, R. Redmer, H. Reinholz, G. Röpke, A. Wierling, S.H. Glenzer, G. Gregori, Plasmon resonance in warm dense matter, Physical Review E 78 (2008) 026411.

[71] T. Döppner, O. Landen, H. Lee, P. Neumayer, S. Regan, S. Glenzer, Temperature measurement through detailed balance in x-ray thomson scattering, High Energy Density Physics 5 (2009) 182–186.

[72] Y. Ping, A. Correa, T. Ogitsu, E. Draeger, E. Schwegler, T. Ao, K. Widmann, D. Price, E. Lee, H. Tamb, P. Springer, D. Hanson, I. Koslow, D. Prendergast, G. Collins, A. Ng, Warm dense matter created by isochoric laser heating, High Energy Density Physics 6 (2010) 246.

[73] P.K. Patel, A.J. Mackinnon, M.H. Key, et al., Isochoric heating of solid-density matter with an ultrafast proton beam, Physical Review Letters 91 (2003) 125004.

[74] G.M. Dyer, A.C. Bernstein, B.I. Cho, et al., Equation-of-state measurement of dense plasmas heated with fast protons, Physical Review Letters 101 (2008) 015002.

[75] A more complete description of the experiment is given in R. Shepherd, et al, Ionization balance and proton stopping power in high-density plasmas, in preparation.

[76] M. Borghesi, J. Fuchs, S.V. Bulanov, et al., Fast ion generation by high-intensity laser irradiation of solid targets and applications, Fusion Science and Technology 49 (2006) 412–439.

[77] J.P. Geindre, P. Audebert, S. Rebibo, J.C. Gauthier, Single-shot spectral interferometry with chirped pulses, Optics Letters 26 (2001) 1612–1614.

[78] P. Antici, J. Fuchs, M. Borghesi, et al., Hot and cold electron dynamics following high-intensity laser matter interaction, Physical Review Letters (2008) 105004.

[79] H. Chen, A. Hazi, R. van Maren, et al., An imaging proton spectrometer for short-pulse laser plasma experiments, Review of Scientific instruments 81 (2010) 10D314.

[80] K. Tiedtke, A. Azima, N. von Bargen, L. Bittner, S. Bonfigt, S. Duesterer, B. Faatz, U. Fruehling, M. Gensch, C. Gerth, N. Guerassimova, U. Hahn, T. Hans, M. Hesse, K. Honkavaar, U. Jastrow, P. Juranic, S. Kapitzki, B. Keitel, T. Kracht, M. Kuhlmann, W. Li, M. Martins, T. Nunez, E. Ploenjes, H. Redlin, E.L. Saldin, E. Schneidmiller, J. Schneider, S. Schreiber, N. Stojanovic, F. Tavella, S. Toleikis, R. Treusch, H. Weigelt, H. Wellhoefer, M. Wabnitz, M. Yurkov, J. Feldhaus, The soft x-ray free-electron laser flash at desy: beamlines, diagnostics and end-stations, New Journal of Physics 11 (2009) 023029.

[81] P. Emma, R. Akre, J. Arthur, R. Bionta, C. Bostedt, J. Bozek, A. Brachmann, P. Bucksbaum, R. Coffee, F.-J. Decker, Y. Ding, D. Dowell, S. Edstrom, A. Fisher, J. Frisch, S. Gilevich, J. Hastings, G. Hays, P. Hering, Z. Huang, R. Iverson, H. Loos, M. Messerschmidt, A. Miahnahri, S. Moeller, H.-D. Nuhn, G. Pile, D. Ratner, J. Rzepiela, D. Schultz, T. Smith, P. Stefan, H. Tompkins, J. Turner, J. Welch, W. White, J. Wu, G. Yocky, J. Galayda, First lasing and operation of an Å ngstrom-wavelength free-electron laser, Nature Photonics 4 (2010) 641–647.

[82] J.N. Glosli, F.R. Graziani, R.M. More, M.S. Murillo, F.H. Streitz, M.P. Surh, L.X. Benedict, S. Hau-Riege, A.B. Langdon, R.A. London, Molecular dynamics

[83] M. Surh, I. Barbee, T.W.,L. Yang, First principles molecular dynamics of dense plasmas, Physical Review Letters 86 (2001) 5958–5961.

[84] P. Hohenberg, W. Kohn, Inhomogeneous electron gas, Physical Review 136 (1964) B864–B871.

[85] N. Mermin, Thermal properties of the inhomogeneous electron gas, Physical Review 137 (1965) A1441–A1443.

[86] R. Feynman, N. Metropolis, E. Teller, Equations of state of elements based on the generalized Fermi-Thomas theory, Physical Review 75 (1949) 1561–1573.

[87] F. Lambert, J. Clerouin, G. Zérah, Very-high-temperature molecular dynamics, Physical Review E (Statistical, Nonlinear, and Soft Matter Physics) 73 (16403) (2006) 1–5.

[88] J. Clerouin, E. Pollock, G. Zerah, Thomas-Fermi molecular dynamics, Physical Review A (Statistical Physics, Plasmas, Fluids, and Related Interdisciplinary Topics) 46 (1992) 5130–5137.

[89] F. Perrot, Gradient correction to the statistical electronic free energy at nonzero temperatures: application to equation-of-state calculations, Physical Review A (General Physics) 20 (1979) 586–594.

[90] F. Perrot, Hydrogen-hydrogen interaction in an electron gas, Journal of Physics: Condensed Matter 6 (1994) 431–446.

[91] H. Feldmeier, J. Schnack, Molecular dynamics for fermions, Review of Modern Physics 72 (3) (2000) 655–688.

[92] A.K. Kerman, S.E. Koonin, Hamiltonian formulation of time-dependent variational principles for the many-body system, Annals of Physics 100 (1976) 332–358.

[93] P. Kramer, A review of the time-dependent variational principle, Journal of Physics Conference Series 99 (2008) 1–8.

[94] J. Broeckhove, L. Lathouwers, E. Kesteloot, P. Van Leuven, On the equivalence of time-dependent variational principles, Chemical Physics Letters 149 (5–6) (1988) 547–550.

[95] E. Heller, Time-dependent approach to semiclassical dynamics, Journal of Chemical Physics 62 (1975) 1544–1555.

[96] D. Klakow, C. Toepffer, P.-G. Reinhard, Semiclassical molecular-dynamics for strongly coupled coulomb-systems, Journal of Chemical Physics 101 (12) (1994) 10766–10774.

[97] D. Klakow, C. Toepffer, P.-G. Reinhard, Hydrogen under extreme conditions, Physics Letters A 192 (1994) 55–59.

[98] R.G. Littlejohn, The semiclassical evolution of wave-packets, Physics Reports 138 (4–5) (1986) 193–291.

[99] M. Griebel, S. Knapek, G. Zumbusch, Numerical Simulation in Molecular Dynamics, Springer-Verlag, 2007.

[100] R. Car, M. Parrinello, Unified approach for molecular dynamics and density-functional theory, Physical Review Letters 55 (22) (1985) 2471–2474.

[101] Y.L. Klimontovich, Statistical Physics, Harwood Academic Publishers, 1982.

[102] P. Carruthers, F. Zachariasen, Quantum collision theory with phase-space distributions, Reviews of Modern Physics 55 (1983) 245–285.

[103] M. Bonitz, Quantum Kinetic Theory, B.G. Teubner, 1998.

[104] R.L. Guernsey, Kinetic theory of quantum plasmas, Physical Review 127 (1962) 1446–1452.

[105] W.R. Chappell, W.E. Brittin, Quantum kinetic equations for a multi-component system of charged particles and photons, Physical Review 146 (1966) 75.

[106] A. Ron, Kinetic equations for electrons and phonons, Journal of Mathematical Physics 4 (1963) 1182.

[107] F. Filbet, E. Sonnendrucker, Comparison of Eulerian vlasov solvers, Computer Physics Communications 150 (3) (2003) 247–266.

[108] P. Reinhard, E. Suraud, On dissipative features of the Vlasov equation.1. Relaxation in Vlasov dynamics, Annals of Physics 239 (2) (1995) 193–215.

[109] R. Illner, G. Rein, Time decay of the solutions of the Vlasov-Poisson system in the plasma physical case, Mathematical Methods in the Applied Sciences 19 (17) (1996) 1409–1413.

[110] H. Struchtrup, Macroscopic Transport Equations for Rarefied Gas Flows: Approximation Methods for Kinetic Theory, Springer-Verlag, Berlin Heidelberg, 2005.

[111] M.D. Feit, J.J.A. Fleck, Wave packet dynamics and chaos in the Hènon-Heiles system, Journal of Chemical Physics 78 (1983) 301.

[112] M.D. Feit, J.J.A. Fleck, Solution of the Schrödinger equation by a spectral method II: vibrational energy levels of triatomic molecules, Journal of Chemical Physics 80 (1984) 2578.

[113] A.D. Bandrauk, H. Shen, Exponential split operator methods for solving coupled time-dependent Schrödinger equations, Journal of Chemical Physics 99 (1993) 1185.

[114] N. Balakrishnan, C. Kalyanaraman, N. Sathyamurthy, Time-dependent quantum mechanical approach to reactive scattering and related processes, Physics Reports 280 (1997) 80.

[115] C. Leforestier, R.H. Bisseling, C. Cerjan, M.D. Feit, R. Friesner, A. Guldberg, A. Hammerich, G. Jolicard, W. Karrlein, H.-D. Meyer, N. Nipkin, O. Roncero, R. Kosloff, A comparison of different propagation schemes for the time dependent Schrödinger equation, Journal of Computational Physics 94 (1991) 59.

[116] E. Wigner, On the quantum correction for thermodynamics equilibrium, Physical Review 40 (1932) 949–759.

[117] G. Box, M.E. Muller, A note on the generation of random normal deviates, The Annals of Mathematical Statistics 29 (1958) 610–611.

[118] C.-Y. Wong, Dynamics of nuclear fluid. VII. Time-dependent Hartree-Fock approximation from a classical point of view, Physical Review C 25 (1982) 1460–1475.

[119] M.P. Allen, D.J. Tildesley, Computer Simulation of Liquids, Oxford Science Publications, Oxford, 1987.

[120] P. Kustaanheimo, E. Stiefel, Perturbation theory of kepler motion based on spinor regularization, Journal für die reine und angewandte Mathematik 218 (1965) 204–219.

[121] M.D. Vivarelli, The KS-transformation in hypercomplex form and the quantization of the negative-energy orbit manifold of the Kepler problem, Celestial Mechanics and Dynamical Astronomy 36 (1985) 349–364.

[122] W. Neutsch, Quaternionic Regularisation of Perturbed Kepler Motion, Max-Planck-Inst. math., Bonn, 2007.

[123] S.J. Aarseth, Direct methods for N-body simulations, in: J. Brackbill, B. Cohen (Eds.), Multiple Time Scales, Academic Press, 1985, pp. 377–418.

[124] S.J. Aarseth, Gravitational N-Body Simulations, Cambridge Monographs on Mathematical Physics, Cambridge University Press, The Edinburgh Building, Cambridge CB2 2RU, UK, 2003.

[125] D. Heggie, P. Hut, The Gravitational Million-Body Problem, Cambridge University Press, The Edinburgh Building, Cambridge CB2 2RU, UK, 2003.

[126] D. Condurache, V. Martinusi, A complete closed form vectorial solution to the Kepler problem, Meccanica 42 (2007) 465–476.

[127] A. Markmann, F. Graziani, V. Batista, Kepler Predictor-corrector algorithm: scattering dynamics with one-over-r singular potentials, Journal of Chemical Theory and Computation in press.

[128] C.-Y. Wong, Explicit solution of the time evolution of the Wigner function, Journal of Optics B: Quantum and Semiclassical Optics 5 (2003) S420–S428.